1

Probing Actinide Bonds in the Gas Phase: Theory and Spectroscopy

Michael C. Heaven[1] *and Kirk A. Peterson*[2]

[1] *Department of Chemistry, Emory University, Atlanta, Georgia, United States*
[2] *Department of Chemistry, Washington State University, Pullman, Washington, United States*

1.1 Introduction

Theoretical studies of actinide compounds have two primary goals. The first is to understand the chemical bonding within these materials and their physical properties. A sub-focus within this task is the elucidation of the roles played by the 5*f* electrons. The second goal is to understand the reactivities of actinide compounds. The long-term objective is to develop reliable computational methods for exploring and predicting actinide chemistry. This is highly desirable owing to the practical difficulties in handling the radioactive and short-lived elements within this family.

Actinides pose a severe challenge for computational quantum chemistry models due to the large numbers of electrons and the presence of strong relativistic effects [1–4]. Although small molecules (di- and tri- atomics that contain just one metal atom) can be explored using rigorous theoretical models, the computational cost of this approach is currently too high for most problems of practical interest (e.g., actinide ions interacting with chelating ligands in solution). Consequently, approximate methods are applied. Ab initio calculations can be accelerated by using a single effective core potential to represent the deeply bound electrons of the metal atom [5, 6]. The relativistic effects are folded into this core potential, and the number of electrons explicitly considered by the calculations is greatly reduced. Semi-empirical density functional theory (DFT) methods offer even better computational efficiency. It is, of course, essential that these approximate methods be tested against both accurate experimental data and the results of rigorous "benchmark" calculations.

There are clear advantages for using data obtained from gas-phase measurements for the comparisons with theory. The ideal situation is to evaluate predictions for the bare molecule against experimental data that are untainted by interactions with solvent molecules or a host lattice. Gas-phase spectroscopy can provide accurate determinations of rotational constants, dipole moments, vibrational frequencies, electronic excitation energies, ionization energies, and electron affinities [7–11]. Information concerning the geometric structure and the electronic state symmetries can be derived from the

Experimental and Theoretical Approaches to Actinide Chemistry, First Edition.
Edited by John K. Gibson and Wibe A. de Jong.

rotational energy level patterns, which can only be observed for the unperturbed molecule. The reactivities of actinide-containing species can also be investigated in the gas phase, under conditions that facilitate theoretical comparisons [8, 12–15]. The majority of this work relies on mass spectrometry for the selection of the reactants and identification of the products. In addition to revealing reaction pathways, mass spectrometric experiments provide critical thermodynamic data, such as bond dissociation and ionization energies.

Over the past 30 years, there has been steady progress in the development of relativistic quantum chemistry methods, combined with a dramatic increase in the speed and capacity of computing platforms. On the experimental side, the application of laser-based spectroscopy, guided ion beam, and ion-trap mass spectrometry has significantly advanced our ability to explore the structure, bonding, and reactivity of actinide species. In this chapter, we present an overview of the theoretical and experimental techniques that are currently being used to gain a deeper understanding of actinides through the studies of small molecules in the gas phase. While some background material is presented, the primary focus is on the techniques that are currently being applied and developed. To limit the scope, the experimental section is strictly devoted to gas-phase measurements. There is a large body of excellent spectroscopic work that has been carried out for actinide species trapped in cryogenic rare-gas matrices. The data from these measurements are also of great value for tests of theoretical predictions, as the rare-gas solid is usually a minimally perturbing host. For a review of the matrix work, see Reference [8]

1.2 Techniques for Obtaining Actinide-Containing Molecules in the Gas Phase

The earliest spectroscopic studies of actinide-containing molecules in the gas phase were carried out using compounds that possessed appreciable vapor pressures at room temperature. Hence, the hexafluorides UF_6, NpF_6 and PuF_6 were studied by conventional spectroscopic means [8], with suitable precautions for handling radionuclides. The tetrahalides have lower room temperature vapor pressures, but workable number densities have been obtained using moderate heating of the samples [8]. Studies of thorium oxide (ThO) emission spectra were carried out using ThI_4 as the source of the metal [16]. This reagent was subjected to a 2.45 GHz microwave discharge that was sustained in approximately 0.1 Torr of Ne buffer gas. The oxide was readily formed by the reaction of the discharge-generated Th atoms with the walls of the quartz tube that contained the ThI_4/Ne mixture. Molecular ions can also be generated at workable number densities using discharges with volatile compounds. An example is provided by the recent study of ThF^+ reported by Gresh et al. [17]. ThF_4 was used as the starting reagent, and the vapor pressure was increased by heating the quartz discharge tube to 1193 K. The tube was filled with approximately 5 Torr of He, and the mixture was excited by an AC discharge operated at a frequency of 10 kHz.

More commonly, actinide species are refractory solids that require somewhat extreme conditions for vaporization. Tube furnaces [18, 19], Knudsen ovens [20, 21], discharge sputtering [14], discharges [16, 17, 22], and laser ablation techniques [8, 23–25] have been successfully applied. High-temperature vaporization is exemplified by

studies of the electronic spectrum of uranium oxide (UO), carried out using a Knudsen oven to vaporize U-metal samples that had been pre-oxidized by exposure to air [21]. The crucible was heated to temperatures in the range of 2400–2600 K. This was high enough that thermally excited electronic transitions could be observed using conventional emission spectroscopy. The UO vapor pressure generated by the Knudsen oven was sufficient for the recording of absorption and laser-induced fluorescence (LIF) spectra. Resistively heated tube furnaces have also been used for studies of gas-phase UO. The advantage of this approach is that it provides a longer optical path length, and thereby yields spectra with greater signal-to-noise ratios. Extensive high-resolution electronic spectra for UO were recorded by Kaledin et al. [18] using a tube furnace that was heated to 2400 K. More recently, Holt et al. [19] have used a tube furnace to record microwave absorption spectra for UO in the 500–650 GHz range. Transitions between the rotational levels of multiple low-lying electronic states (including the ground state) were observed.

Many of the early mass spectrometric studies of gas-phase actinide molecules were carried out using thermal vaporization in combination with electron impact ionization techniques [26–28]. Surface ionization of uranyl acetate has been used to generate UO^+ and UO_2^+ [29]. In the thorium ion experiments of Armentrout et al. [14, 30], thorium powder was mounted in a cathode held at −2.5 kV. This electrode produced a discharge in a flow of Ar, and the resulting Ar^+ ions generated Th^+ by sputtering. Molecular ions, such as $ThCH_4^+$, were formed in a downstream flow tube. These techniques are suitable for measurements that rely on charged particle detection, but the number densities are usually too small for conventional spectroscopic observations (e.g., absorption or fluorescence detection).

For spectroscopic techniques that are compatible with pulsed generation of the target species, laser vaporization has proved to be a particularly versatile method. The products include cations, anions, and molecules in exotic oxidation states. Duncan [23] has published a very informative review of this technique. Typically, a pulsed laser (Nd/YAG or excimer with 5–10 ns pulse duration) is focused onto the surface of a target to produce a vapor plume. The products are cooled and transported using a flow of an inert carrier gas (e.g., He or Ar). If the plume does not contain the species of interest, the carrier gas can be seeded with a reagent that will produce the desired product. For example, gas-phase UF has been produced by vaporizing U metal into a flowing mixture of He and SF_6 [31].

Charged species are produced by the vaporization process, even in the absence of an externally applied electric field. Cations are formed by thermal processes and photoionization. Some of the liberated electrons attach to neutral molecules, providing a viable flux of negative ions under suitable conditions. External fields can be applied if the initial ion yield is not high enough for the detection technique.

A particularly valuable advantage of the laser vaporization technique is that it can be readily combined with a supersonic jet expansion nozzle. Figure 1.1 (reproduced from Reference [23]) shows this combination for a pulsed solenoid gas valve (labeled "General Valve"). The valve supplies a high-pressure pulse of carrier gas, timed to coincide with the laser vaporization pulse. The entrained plume passes through a reaction channel before expansion into a vacuum chamber. On expansion, the gas temperature and density drops rapidly. The internal degrees of freedom for entrained molecules can be relaxed to population distribution temperatures in the range of 5–20 K. Condensation

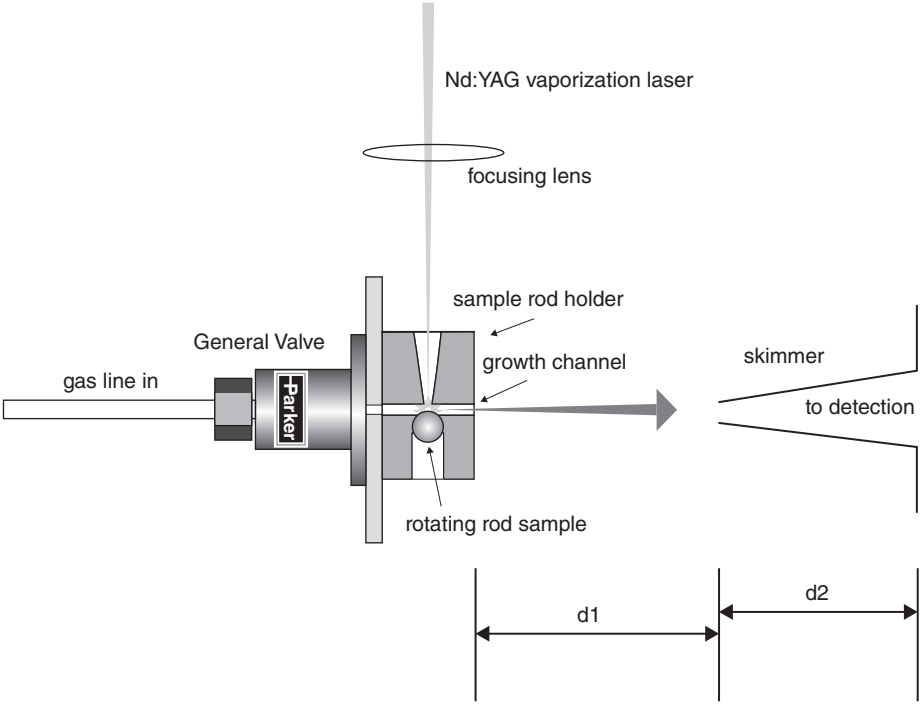

Figure 1.1 The general schematic design of a "standard" laser vaporization cluster source (Reproduced with permission from Duncan, M.A. (2012) Invited review article: Laser vaporization cluster sources. *Review of Scientific Instruments*, **83**, 041101/1–041101/19.)

is prevented by the concomitant drop in gas density. The cooling greatly facilitates spectroscopic studies by dramatically reducing the number of thermally populated internal energy states. In this context, it is useful to note that the rapid expansion often leads to non-equilibrium population distributions. Collisional relaxation rates are sensitive to the energy spacings between levels, and they are most favorable for the smallest energy intervals (provided that there are no symmetry restrictions involved). Transfer between the closely spaced rotational levels is facile. Consequently, low rotational temperatures are easily attained. The more widely spaced vibrational levels require a larger number of collisions for effective relaxation. As the number of collisions is limited by the expansion kinetics, the final population distribution will often show a vibrational temperature that is substantially higher than the rotational temperature. Lastly, the pulsed vaporization process can populate metastable electronically excited states, which can be quite resistive to cooling in the expansion. A study of the jet-cooled Be_2 dimer illustrates this hierarchy [32]. The rotational temperature was 7 K, the vibrational temperature was near 160 K, and an electronically excited triplet state with an energy of 7406 cm^{-1} was substantially populated.

The gas dynamics can also be used to exert some control over the chemistry occurring in the expansion. One way this can be accomplished is by varying the length of the "growth channel" as shown in Figure 1.1. Lengthening this channel increases the time for which the density of reactive species is high enough for chemistry to occur. As a

simple example, clusters of metal atoms are often seen following vaporization of a metal target. The mean size of the clusters increases with the length of the growth channel. There are several other factors that influence the chemistry. These include the concentrations of reactants added to the carrier gas, the laser power, wavelength, and pulse duration. Duncan [23] provides a helpful discussion of the effects of these parameters.

Electrospray ionization (ESI) provides a versatile means of producing both cations and anions in the gas phase [33]. ESI is a soft ionization method that can produce complex ions that would not survive the harsh conditions of thermal vaporization or laser ablation. Multiply charged ions can be made, along with partially solvated species that yield insights concerning solution phase speciation. For this technique, actinide salts are first dissolved in a polar solvent (e.g., water, methanol, or acetonitrile). The solution is then forced through a metal capillary tube that is held at a high voltage (on the order of a few kilovolts). Ionization and droplet fragmentation occurs as the liquid exits the capillary tube. The products are de-solvated and then sampled into ion traps and/or mass spectrometers. Gibson and coworkers [10, 13, 34–41] have made extensive use of ESI to study reactions of both bare and solvated actinide ions. Gibson's laboratory has the rare capability of handling samples that are radiologically challenging (e.g., Pa, Pu, Am, and Cm). Spectroscopic studies of cations produced by ESI have been performed by means of action spectroscopy, which permits the application of charged particle detection [24, 42–48]. Anions can also be produced by ESI and characterized by photoelectron spectroscopy. Wang [33] has recently reviewed the application of these techniques to actinide-containing anions.

1.3 Techniques for Spectroscopic Characterization of Gas-Phase Actinide Compounds

1.3.1 Conventional Absorption and Emission Spectroscopy

The volatile hexafluorides UF_6, NpF_6, and PuF_6 have been examined using IR and optical absorption spectroscopy [8, 49–55]. Data for these molecules, recorded under room temperature conditions, are complicated by the thermal population of many low-energy ro-vibronic states. For example, it has been estimated that 99.6% of UF_6 molecules populate vibrationally excited levels at 300 K [53, 56]. This problem has been partially mitigated by working with low-temperature cells, but the temperature dependence of the vapor pressure imposes a practical lower limit of about 160 K. Lower temperatures have been achieved for UF_6 using isentropic gas expansion techniques [57, 58]. Due to the large flow rates needed for this technique, it does not appear to have been applied to NpF_6 or PuF_6. Electronic spectra for the hexafluorides have been examined at room temperature, but the level of congestion yields data that are difficult to assign.

Electronic emission spectra for ThO and UO have been recorded using standard monochromators for dispersion. Thermal excitation of UO [21] and discharge excitation of ThO [16, 59–67] yielded emission intensities that were sufficient for the recording of spectra at the Doppler limit of resolution. Rotationally resolved electronic spectra have been obtained over the range from the near-UV to the near-IR. In these studies, the data were recorded by means of photographic plates or high-gain photomultiplier tubes. Owing to the high-temperature source conditions, many levels of the oxides were significantly populated. In the case of UO, Kaledin et al. [21] reported seeing approximately 500 vibronic bands

within the 400–900 nm range. Despite this complexity, several assignable bands were identified. This was possible due to the relatively large rotational constants of the monoxide. Kaledin et al. [21] were also able to record absorption spectra for UO using a continuum light source (Xenon lamp) and a monochromator.

Pure rotational spectroscopy, conducted in the microwave and sub-millimeter wave regions, can provide some of the most accurate molecular constants. At these low transition energies, both the Doppler and lifetime broadenings of the spectral lines are smaller by orders of magnitude, as compared to the visible region. This is conveniently exemplified by UO. For the experiments of Kaledin et al. [21], the Doppler width near 500 nm was 1.3 GHz, and the natural linewidth was approximately 1 MHz. By contrast, the sub-millimeter spectrum of UO, recorded by Holt et al. [19] at a temperature of 2200 K, had a Doppler linewidth of 1.3 MHz, and the natural linewidth was below the effects of pressure broadening. The sub-millimeter wave data for UO were recorded using a frequency modulation technique, and over 280 lines were observed within the 510–652 GHz range. Prior to this study, Cooke and coworkers [68–70] were the first to obtain a microwave spectrum for an actinide-containing molecule (ThO). For these measurements, they used laser ablation and jet expansion cooling to obtain cold gas-phase samples of ThO. A cavity-enhanced absorption technique was used to achieve high sensitivities. Pulsed excitation was used, and the spectra were recovered via Fourier analysis of the time-dependent response. Due to the non-equilibrium nature of jet cooling, they were able to record the pure rotational lines ($J = 0 \rightarrow 1$) for $^{232}Th^{16}O$ vibrational levels ranging from $v = 0$ to 11 (transitions of the $Th^{17}O$ and $Th^{18}O$ isotopes were also examined for lower vibrational levels).

1.3.2 Photoelectron Spectroscopy

Gas-phase photoelectron spectra have been recorded for a small number of Th and U compounds, including UO, UO_2 [71], UF_6 [72], ThX_4, and UX_4 (X = F, Cl, and Br) [73–76]. The vapors were generated by heating solid samples, and the molecules were ionized by means of monochromatic VUV light (e.g., the He II line at 40.8 eV). Ionization energies and spectra for the molecular ions were derived by measuring the kinetic energy distributions of the photoelectrons. This was accomplished using a hemispherical electrostatic analyzer, which is capable of resolving down to about 40 cm^{-1}. This is sufficient to distinguish well-separated vibrational levels and electronically excited states. However, the actinide ions often possess multiple low-lying electronic states, due to the presence of partially filled *d*- or *f*- orbitals on the metal. For molecular ions such as UO^+ and UO_2^+, the low-energy vibrational states are so dense that their photoelectron spectra yield broad, unresolved features [71]. A summary of the gas-phase photoelectron studies of simple actinide compounds is given in Reference [8]. Higher-resolution data for molecular ions have since been obtained using the laser-based methods described in the following sections.

1.3.3 Velocity Modulation and Frequency Comb Spectroscopy

Spectroscopic studies of molecular ions are challenging due to the low densities at which ions can be generated. The concentrations are limited by the reactive nature of the ions, and their Coulombic repulsion. Consequently, ions are nearly always accompanied by

much higher concentrations of neutral molecules. In most instances, the spectra for the neutrals will mask the much weaker signals from the ions. One solution to this problem is to use velocity modulation of the ions [77–79]. This technique requires a tunable laser light source that has a linewidth that is comparable to or smaller than the Doppler linewidth of the transition of interest. Ions are generated in a discharge tube using an alternating current with a frequency in the kilohertz range. During each cycle, the ions are accelerated back and forth along the tube. The laser is propagated along the tube axis, and the transmitted intensity is monitored. If the laser is tuned to the edge of an absorption line, the transmitted intensity will be modulated as the ions are Doppler-tuned in and out of resonance. By observing the signal at the modulation frequency (or multiples thereof), the detection can be strongly biased in favor of the ions (transient neutral species may still be detected due to concentration modulation)[79].

Due to the narrow linewidth required for the velocity modulation technique, scanning for new spectral features is a time-consuming process. A dramatic improvement in the data acquisition rate has recently been achieved by combining velocity modulation with frequency comb spectroscopy (for a detailed review of the frequency comb technique, see Reference [80]). Briefly, a femtosecond pulsed laser with a stabilized optical cavity is used to generate a "comb" of laser frequencies. The frequency spacing of the comb is determined by the cavity round trip time, and the comb contains around 10^5 individual frequencies. This radiation is transmitted through the sample, and dispersed using the combination of a virtually imaged phased array (VIPA) disperser (high resolution) and a diffraction grating (low resolution). By this means, every element of the frequency comb is resolved, and their transmitted intensities are recorded. For the detection of ions, velocity modulation and a multipass optical cavity are employed. Figure 1.2 shows the apparatus used by Gresh et al. [17] to record high-resolution spectra for the ThF^+ ion. Bands that were tentatively assigned to the ThO^+ ion were also present in these spectra. Cossel et al. [22] found that data acquisition with the frequency comb system was about 30 times faster than with conventional velocity modulation spectroscopy. To date, ThF^+ is the only actinide-containing species examined using frequency comb spectroscopy. However, it is evident that a wide range of actinide species (ions and neutrals) could be studied using this powerful tool.

1.3.4 LIF Spectroscopy

LIF spectroscopy of electronic transitions is a versatile method that can achieve high resolution (including methods for overcoming Doppler broadening) [79]. In its simplest form, LIF is performed by tuning a laser through absorption bands and detecting the resulting fluorescence without active selection of the detected wavelengths (usually the optical filter used to block scattered laser light, and the characteristics of the photodetector determine the part of the emission spectrum that is most effectively detected). The result is essentially the absorption spectrum, convoluted with the fluorescence quantum yield for the excited state. Pulsed laser excitation works well, and is readily combined with pulsed laser ablation sources. To illustrate the technique, Figure 1.3 shows the main components of the apparatus at Emory University that is used to study the electronic spectra of actinide-containing molecules. The first vacuum chamber of this instrument houses a laser ablation/jet cooling nozzle source. The beam from a pulsed dye laser crosses the expanding jet a few centimeters downstream from the

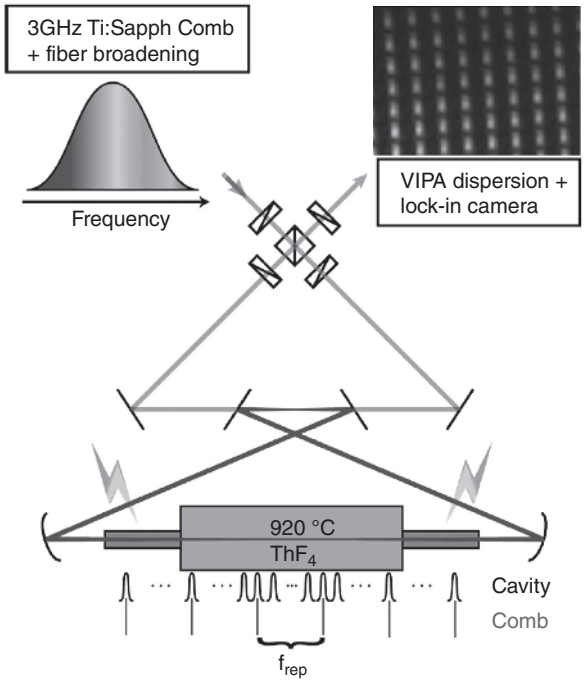

Figure 1.2 The frequency comb/velocity modulation spectrometer. A 3 GHz Ti:Sapphire comb is broadened by a nonlinear fiber and coupled into a bow-tie ring cavity, propagating in either direction through a discharge of ThF_4. Four liquid crystal variable retarders and a polarizing beam splitter control the direction of light propagation through the discharge. After exiting the cavity, the laser light is sent to a cross-dispersive VIPA imaging system with single comb mode resolution and imaged onto a lock-in camera. Approximately 1,500 comb modes are resolved in a single image. (Reproduced with permission from Gresh, D.N., Cossel, K.C., Zhou, Y., Ye, J., and Cornell, E.A. (2016) Broadband velocity modulation spectroscopy of ThF^+ for use in a measurement of the electron electric dipole moment. *Journal of Molecular Spectroscopy*, **319**, 1–9.)

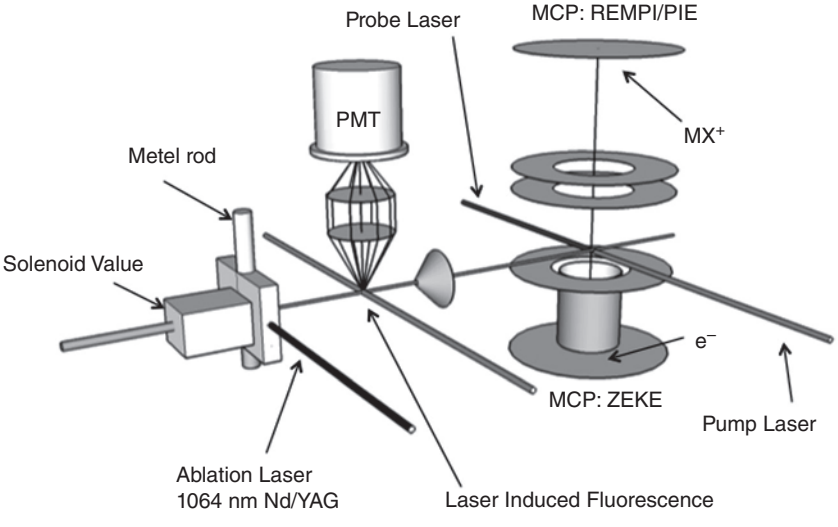

Figure 1.3 Schematic diagram of an apparatus used to record LIF, resonantly enhanced multiphoton ionization (REMPI), PIE, and PFI-ZEKE spectra for gas-phase actinide molecules.

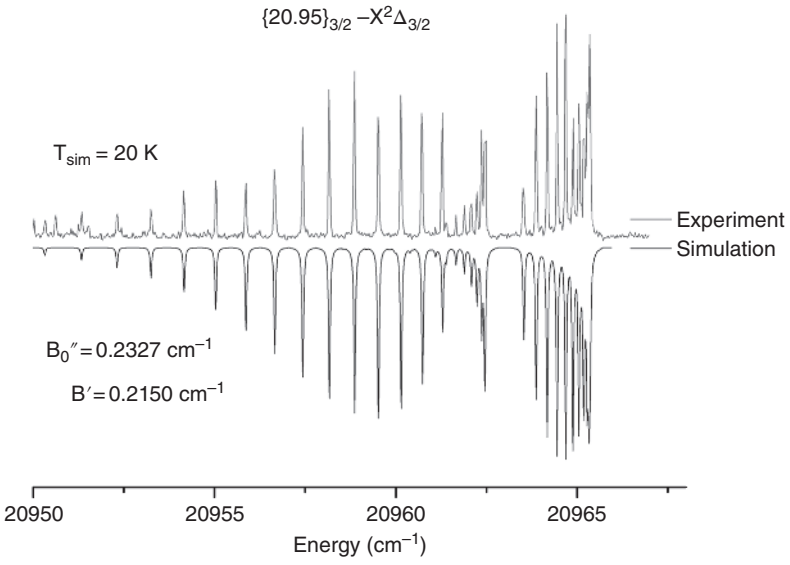

Figure 1.4 Rotationally resolved laser-induced fluorescence (LIF) spectrum of the ThF {20.95}3/2-$X^2\Delta_{3/2}$ band. The downward-going trace is a computer simulation. (*See insert for color representation of the figure.*)

nozzle orifice. The resulting fluorescence is detected along an axis that is perpendicular to the gas flow direction and the probe laser beam. Figure 1.4 shows representative data for ThF. Here, it can be seen that the rotational temperature is low (around 20 K), and the rotational structure is resolved. Note, however, that small splittings associated with breaking of the electronic degeneracy (Ω-doubling) and the hyperfine structure resulting from the nuclear spin of the F atom are not resolved. An advantage of pulsed laser excitation is that the fluorescence can be time-resolved, thereby providing information concerning the lifetimes and transition moments of the excited states.

The resolution of the spectrometer shown in Figure 1.3 is ultimately limited by two constraints. The first is the use of incoherent pulsed laser excitation, which cannot provide a linewidth that is less than that defined by the Fourier transform of the temporal pulse shape. The second limitation is from Doppler broadening. Although the internal temperature within the supersonic flow is low, the molecules are accelerated by the carrier gas as the expansion evolves. If a wide angular spread of the jet is probed by the laser, the supersonic flow velocity (on the order of 1760 ms^{-1} for He) results in appreciable line broadening. This effect can be mitigated by either skimming the core of the expansion into a second vacuum chamber prior to laser excitation, or by masking the fluorescence detection system such that only molecules with low velocities along the laser axis can be observed (a simple slit mask is sufficient). The problem with the laser linewidth can be overcome by switching to a tunable continuous wave (CW) laser. Despite the typically low duty cycle of pulsed laser ablation sources, LIF detection has a high enough sensitivity that the use of a CW probe laser is viable.

The combination of a skimmed molecular beam and a narrow linewidth CW probe laser has been applied to the study of actinide-containing molecules by Steimle and coworkers. To date, this system has been used to examine electronic transitions of ThO

[81], ThS [82], UO [83], and UF [84]. The resolution achieved (around 40 MHz) has been close to the limit imposed by the natural linewidth ($\Delta\nu = \frac{1}{2\pi\tau}$, where τ is the excited state lifetime). This high resolution has permitted measurements of line splitting induced by externally applied electric and magnetic fields. These data yield accurate values for the electric and magnetic dipole moments of both the upper and lower electronic states.

LIF spectra of jet-cooled molecules yield extensive information on electronically excited states, but the data for the ground state may be limited to the properties of the zero-point level. A more extended view of the electronic ground state can be obtained by spectral resolution of the LIF (referred to as dispersed fluorescence in the following text). In addition, the dispersed fluorescence spectra may also reveal the presence of low-energy electronically excited states. Such measurements are particularly effective when the excitation laser is tuned to a single vibronic level of an electronically excited state. The range of ground state vibrational levels observed is dictated by the square of the overlap integral between the upper and lower state vibrational wavefunctions (the Franck–Condon factors). When other electronic states are present, transitions to those that satisfy the usual selection rules are observed. As an example, Figure 1.5 shows a dispersed fluorescence spectrum for ThS, obtained by exciting an upper electronic state with $\Omega = 1$ (where Ω is the unsigned projection of the electronic angular momentum along the bond axis) [85]. The bands on the left-hand side of this spectrum reveal the vibrational structure of the $X^1\Sigma^+$ ground state, while the bands at higher energy are for the $^3\Delta_1$ and $^3\Delta_2$ excited states (the third component of the triplet, $^3\Delta_3$, was not observed as the selection rule is $\Delta\Omega = 0, \pm 1$). The range of levels observed in the dispersed fluorescence spectrum can be manipulated, to some extent, through the choice of the initially excited level.

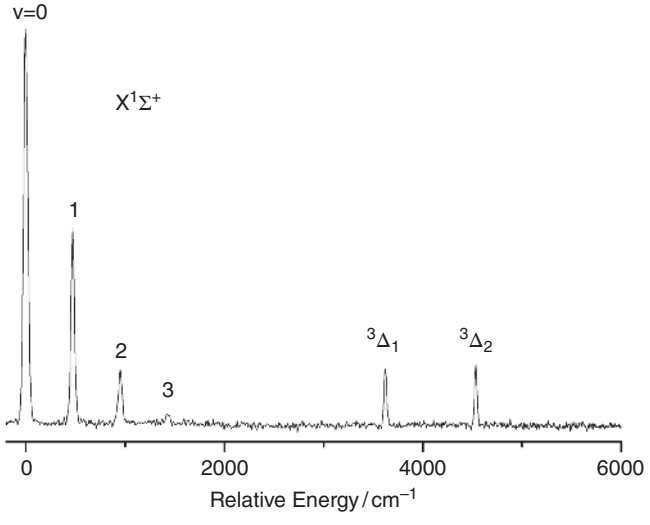

Figure 1.5 Dispersed fluorescence spectrum for ThS recorded using laser excitation of the [22.13]1-$X^1\Sigma^+$ band. (Reproduced with permission from Bartlett, J.H., Antonov, I.O., and Heaven, M.C. (2013) Spectroscopic and Theoretical Investigations of ThS and ThS^+. *Journal of Physical Chemistry A*, **117**, 12042–12048.).

The combination of laser excitation with dispersed fluorescence detection can be used as a two-dimensional method in order to disentangle complex and congested spectra [79]. There are typically two sources of complexity. In laser ablation/jet cooling experiments, the control over the species created is somewhat limited. Consequently, the spectra may include features from several different molecules. The problem is compounded when thermal vaporization or discharge methods are used to obtain gas-phase species. Many states are populated under these conditions, often leading to severe spectral congestion. The dispersed fluorescence technique described earlier, carried out with a fixed excitation wavelength, shows lower state energy levels that are related through their connection to a common upper level. Provided that a sufficiently narrow linewidth is used in excitation, the emission spectrum for a single molecular component of a mixture can be obtained. Once the pattern of low-lying vibronic states has been established, the spectral scanning procedure can be permuted (fix the monochromator, scan the dye laser) or carried out as a coordinated sweep of both the laser and monochromator wavelengths. Spectra recorded with wavelength-selected fluorescence detection (monochromator fixed) show transitions to a specific upper state. This is almost the same information that is obtained using dispersed fluorescence, but restricted to lower levels that are significantly populated. However, a much higher resolution can be achieved via control of the laser linewidth. The excitation spectrum of a specific molecular species, sought under conditions where other species with overlapping spectra are present, can be obtained by a coordinated scan of both the laser and monochromator wavelengths. The tuning rates for both instruments are calculated to keep the energy difference between the absorbed and emitted photons equal to a lower state interval.

An LIF study of the ThF^+ ion illustrates the value of the two-dimensional approach [86]. In these experiments, ThF was generated by laser ablation of Th in the presence of SF_6. Although ThF^+ ions were surely generated by this means, they were not present at a concentration that was sufficient for LIF detection. Additional ThF^+ ions were generated in the downstream region of the jet expansion by means of pulsed laser ionization. The challenge for this experiment was that both ThF and ThF^+ have many overlapping bands in the visible range. ThF dominated the ordinary LIF spectrum, as only a small fraction of the initial ThF was ionized. A further complication was the presence of many intense ThO bands. Metal oxides are nearly always present in laser ablation experiments, and they are very difficult to suppress. Even when high-purity oxygen-free gasses are used, the oxides are routinely observed. The spectrum of ThF^+ was separated from the interfering bands of ThF and ThO by means of the differences in their ground state vibrational intervals ($\Delta G_{1/2}(ThF^+) = 605, \Delta G_{1/2}(ThF) = 653, \Delta G_{1/2}(ThO) = 891\ cm^{-1}$). The clean ThF^+ LIF spectrum shown in Figure 1.6 was obtained with the monochromator set to observe fluorescence that was $605\ cm^{-1}$ red-shifted relative to the excitation energy [86].

So far, we have described the two-dimensional technique as the sequential recording of one-dimensional cuts (fixed laser or fixed monochromator wavelength slices). This strategy is successful, but the rate of data acquisition is slow. In recent years, the technique has been improved by using monochromators equipped with CCD cameras to record the emission spectrum for each point in the laser excitation spectrum (a method that is conveniently combined with pulsed laser excitation). This allows for a more detailed spectral map to be assembled within a reasonable acquisition time. Recent

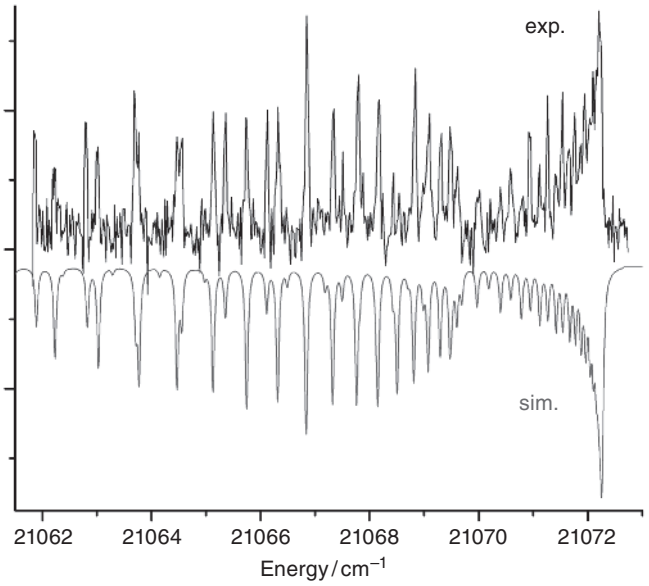

Figure 1.6 Rotationally resolved LIF spectrum of the ThF^+ $[21.1]0^+$-$X^3\Delta_1$ band. The downward-going trace is a computational simulation of the band. (*See insert for color representation of the figure.*)

work by the Steimle group on the first LIF detection of Th_2 illustrates the advantages of this enhancement [87]. The dimer was produced by pulsed laser vaporization of Th metal. As usual, the LIF spectrum, without wavelength selection of the emission, contained many intense bands of ThO. Figure 1.7 shows the two-dimensional spectrum, where a 2000 cm^{-1} segment of the emission spectrum was recorded for every excitation wavelength sampled. Identification of the Th_2 bands in the two-dimensional map is straightforward. Owing to the low vibrational frequency of Th_2, every band of this molecule produces a characteristic column of features. Recording the fluorescence spectrum using the CCD array also facilitates the characterization of relative transition probabilities, as the relative intensities are immune to drifts in the source conditions [88].

1.3.5 Two-Photon Excitation Techniques

The LIF techniques described earlier rely on one-photon excitation processes. With the high intensities provided by lasers and related coherent light sources, there are many two-photon excitation processes that can be exploited. Two-dimensional techniques can be applied if independently tunable light sources are used.

A recent example of a two-photon excitation measurement is the microwave-optical double resonance (MODR) study of ThS reported by Steimle et al. [89]. The MODR technique is a well-established method for recording microwave spectra with a sensitivity that is determined by the electronic transition (electronic transition probabilities are typically orders of magnitude larger than rotational transition probabilities). Figure 1.8 shows the essential components of the MODR experiment. The molecules of interest are entrained in a molecular beam, and a CW laser is used to excite a single rotational line of an electronic transition. The laser beam is divided into two, so that the

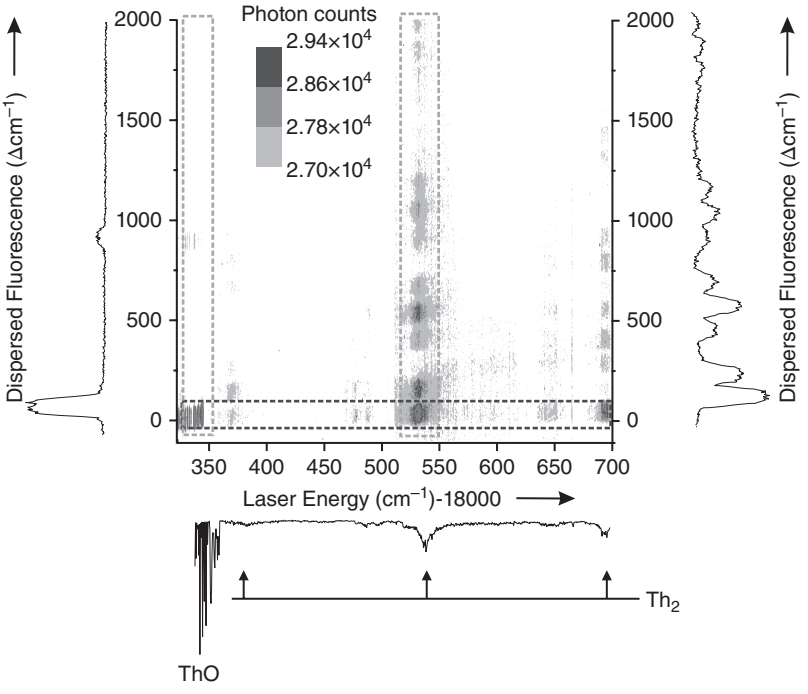

Figure 1.7 2D spectrum over the 18325 – 18700 cm^{-1} laser excitation range of ablated thorium in the presence of a SF6/Ar mixture. Not corrected for laser power variation or the spectral response of the CCD. At the bottom is the on-resonance detected laser excitation spectrum obtained from the vertical integration of the intensities of the horizontal slice marked by the dashed blue rectangle. At the left and right are the dispersed fluorescence spectra resulting from excitation of the (0,0) $F^1\Sigma(+) - X^1\Sigma^+$ band of ThO at 18340 cm^{-1} and Th_2 band at 18530 cm^{-1}, respectively, obtained by horizontal integration of the intensities of the left and right horizontal slices marked in red. (Reproduced with permission from Steimle, T., Kokkin, D.L., Muscarella, S., and Ma, T. (2015) Detection of thorium dimer via two-dimensional fluorescence spectroscopy. *Journal of Physical Chemistry A*, **119**, 9281–9285.) (*See insert for color representation of the figure.*)

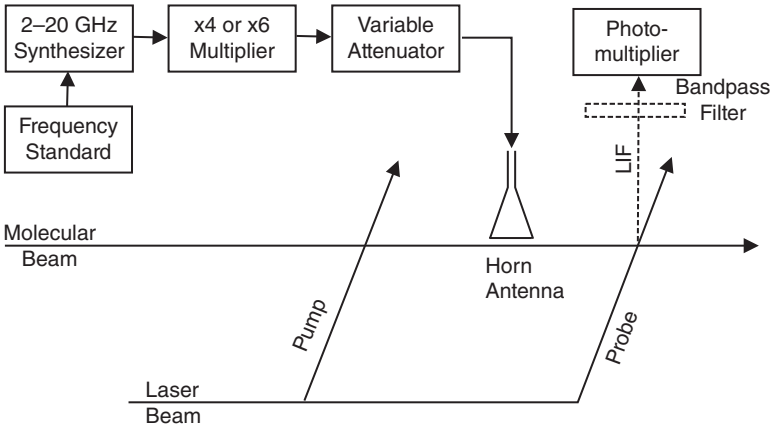

Figure 1.8 A block diagram of the MODR spectrometer. (Reproduced with permission from Steimle, T.C., Zhang, R., and Heaven, M.C. (2015) The pure rotational spectrum of thorium monosulfide, ThS. *Chemical Physics Letters*, **639**, 304–306.)

molecular beam can be excited at two different locations. Most of the power is in the laser beam that is first to intersect the molecular beam. This is used to deplete the population of the rotational state (J) from which excitation occurs. Some distance downstream, the weaker component of the laser beam is used to excite the same rotational line, and the intensity of the fluorescence from this second excitation is monitored. Between the two laser beams, the molecular beam is excited by microwave radiation. When this is resonant with the $J-1 \rightarrow J$ transition, the population transfer increases the LIF signal. By this means, Steimle et al. [89] were able to record pure rotational transitions for ThS ranging from $J=7$ to $J=14$, with a linewidth of 25 kHz. Previous attempts to record the ThS microwave spectrum by using the one-photon excitation techniques that yielded spectra for ThO were unsuccessful. The dipole moment of ThS [82] is slightly larger than that of ThO [81], so it seems that the problem was the production of ThS by laser ablation. We have found that it is easier to make actinide oxides and fluorides with laser ablation, as compared to other chalcogenides or the heavier halogens. The high sensitivity of the MODR method compensates for the low chemical yield, permitting microwave studies of species that are more challenging for gas-phase production.

Resonantly enhanced two-photon ionization techniques have proved to be particularly useful for studies of actinide-containing molecules [7–9]. These methods have the advantage that they can be combined with the mass-resolved detection of ions. In many cases, this mass filter can extract the spectrum for a single species from a complex chemical environment. It can also be used to separate spectra of isotopes, where small isotopic shifts result in congested LIF spectra. Note also that methods that utilize charged particle detection can be far more sensitive than those based on fluorescence detection [79].

The apparatus shown in Figure 1.3 is a typical setup for the recording of mass-resolved, resonantly enhanced multiphoton ionization (REMPI) spectra. The supersonic jet from a laser ablation source is skimmed into the second differentially pumped vacuum chamber (right-hand side of Figure 1.3), forming a well-defined molecular beam. The second chamber houses the components of a Wiley-McLaren time-of-flight mass spectrometer (TOF-MS). Two overlapping pulsed laser beams traverse the molecular beam near the center of the TOF-MS. The lasers have pulse durations of approximately 10 ns, and their synchronization is controlled by a precision pulse delay generator. The ions produced by photoionization are deflected into the flight tube by voltages applied to the repeller and draw-out grids. They are detected by microchannel plates. With a flight path of 40 cm, this system achieves near-unit-mass resolution for masses near 250 amu.

With sequential excitation, there are two options for recording REMPI spectra. In the first scheme, the first laser excites the molecule via a resonant transition. The second laser operates at a fixed photon energy that is high enough to ionize the excited molecules, but not sufficient to ionize from the ground state. The wavelength of the first laser is scanned, and the ion of interest is monitored using the mass spectrometer. It is, of course, straightforward to record the spectra associated with every observed mass peak independently, in a single spectral sweep. The data obtained are equivalent to the absorption spectra for the neutral molecules.

Conversely, the first laser can be fixed on a resonant transition and the second laser scanned in order to locate the ionization threshold (the plot of ion current versus photon energy is often referred to as a photoionization efficiency (PIE) curve).

This measurement can provide a reasonably accurate ionization energy, with uncertainties on the order of $\pm 30\,cm^{-1}$ (± 4 meV). The choice of the first laser resonance can be used to ensure that the signal is exclusively associated with ground state molecules (often a particular rotational level of the zero-point level). Tuning the second laser above the ionization limit can result in a very structured spectrum. The structure is due to the presence of strong auto-ionizing resonances that are embedded in the ionization continuum. The resonances are members of Rydberg series that converge to the rovibronic states of the molecular ion. The high-*n* Rydberg states that exist just beneath each threshold for producing the ion in a particular *v, J* state are unusually long-lived. This property can be exploited in order to obtain spectroscopic data for the molecular ion, using a technique known as pulsed-field ionization zero electron kinetic energy (PFI-ZEKE) spectroscopy [90–92]. In this experiment, a pulsed laser is used to excite the molecule to a small group of high-*n* Rydberg states under field-free conditions. For final ion states that lie above the ionization threshold (e.g., MX^+ $v = 1$), the laser pulse will also cause direct photoionization and rapid auto-ionization. Electrons that are produced by these fast processes are allowed to dissipate during a time interval of a few microseconds. A weak pulsed electric field is then applied. Molecules that are in the high-*n* Rydberg states are ionized by this pulse, and the electrons are accelerated to a microchannel plate detector. Note that PFI-ZEKE spectroscopy can be carried out using single-photon excitation, but the resolution is substantially improved if resonant two-color excitation is employed. The resolution of the two-photon technique, which is determined by the magnitude of the pulsed field, can be as low as $0.5\,cm^{-1}$. These measurements provide accurate ionization energies and well-resolved spectra for the molecular ions. Rotational resolution has been achieved for diatomic ions.

A valuable facet of the PFI-ZEKE technique is that there are few selection rules governing the ion final states can be observed. For example, Goncharov et al. [93] were able to characterize ten low-lying electronic states of UO^+, with Ω values ranging from 0.5 to 5.5. The ability to recover complete maps of low-lying states has proved to be critical for obtaining a deeper understanding of actinide bonding motifs. Such studies of UO^+ and UF^+ [31] show that the U 5*f* orbitals do not participate significantly in the bonding of these ions.

1.3.6 Anion Photodetachment Spectroscopy

Just as PFI-ZEKE spectroscopy can provide information on the low-lying states of a molecular cation, anion photodetachment spectroscopy can reveal the low-energy states of a neutral molecule [33, 94–96]. An advantage of working with anions is that the species of interest can be mass-selected prior to laser excitation. The study of small metal clusters illustrates problems that can be circumvented by working with anions. Previously we have attempted to record spectra for Th_n and U_n with n = 2 or 3 using the mass-resolved REMPI method, in the hope of probing actinide metal–metal bonds. The target ions were readily observed, but their visible range excitation spectra did not exhibit a resolvable structure. Larger metal clusters were present in the laser ablation plume, and it is most probable that these clusters suffered facile multiphoton fragmentation processes. This caused the effectively featureless spectra of the larger clusters to contribute to the signal from the M_2^+ and M_3^+ ions. This problem can be averted when mass selection can be applied prior to laser excitation.

Anion photodetachment measurements use a fixed wavelength laser for detachment. The ejected electrons have kinetic energies (eKE) that are determined by the expression

$$eKE = h\upsilon - EA - E_{Int} \tag{1.1}$$

where hυ is the photon energy, EA is the electron affinity of the neutral molecule, and E_{Int} is the internal energy of the neutral molecule (this model assumes that the anions are cooled to a low internal temperature prior to photodetachment). Hence, the electron kinetic energy distribution encodes the internal energy states of the molecule. A variety of methods have been used to measure the electron kinetic energy distributions. This proves to be a technically challenging problem that is usually the step that limits the resolution. Prior to the development of electron imaging methods, magnetic bottle spectrometers were state of the art, achieving resolutions on the order of 5–10 meV (40–80 cm^{-1}). A considerable improvement in resolution, down to a few cm^{-1}, has been realized by using velocity-map imaging techniques to characterize the detached electrons [94, 95]. With this method, an electrostatic lens is used to project the photodetached electrons along the axis of a flight tube, and image them on a position-sensitive detector (MCPs combined with a phosphor screen and a digital camera). To facilitate the description of this method, Figure 1.9 shows the velocity-map imaging spectrometer used by Wang and coworkers [95].

The components on the left-hand side of this diagram (up to the valve labeled GV2) are used for generation of the anions by laser ablation, followed by time-of-flight mass selection of the target anion. The components for velocity-map imaging (VMI) are housed in the final chamber on the right-hand side of the figure. To understand the images that this instrument produces, consider a photodetachment process that ejects electrons without a preferred direction (isotropic angular distribution). The electrons associated with a specific final state of the molecule will have a fixed velocity, and their

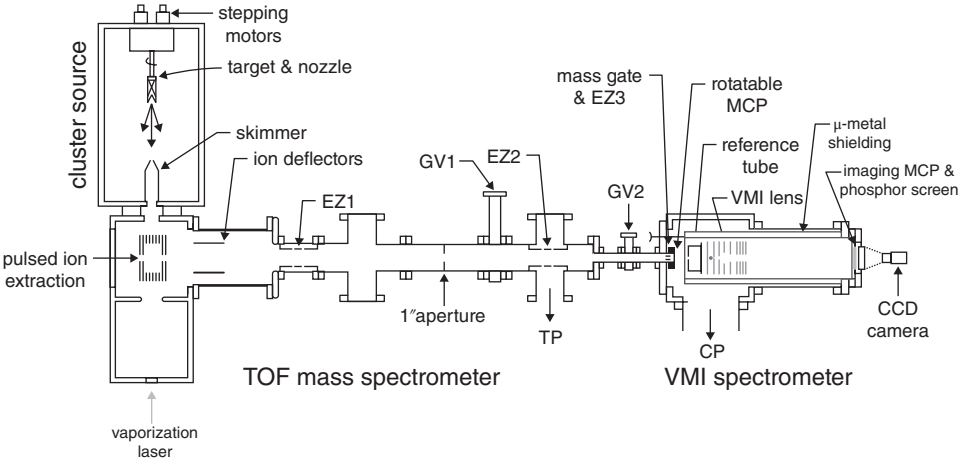

Figure 1.9 Overall schematic view of the high-resolution photoelectron spectroscopy apparatus for size-selected clusters using velocity-map imaging (VMI). (Reproduced with permission from Leon, I., Yang, Z., Liu, H.-T., and Wang, L.-S. (2014) The design and construction of a high-resolution velocity-map imaging apparatus for photoelectron spectroscopy studies of size-selected clusters. *Review of Scientific Instruments*, **85**, 083106/1–083106/12.)

radial distance from the point of detachment will increase linearly with time (an expanding sphere of electrons). This group of electrons is projected along the flight tube at a velocity that is determined by the biasing of the electrostatic (VMI) lens. When the electrons reach the detector, they produce a disk image owing to the reduction of the three-dimensional spatial distribution to a two-dimensional image. The diameter of this disc is determined by the electron kinetic energy and the time needed to travel to the detector. If multiple final states of the molecule are produced, the image consists of multiple concentric discs. The use of linearly polarized laser light can produce spatial velocity distributions that are cylindrically symmetric about the polarization vector, but otherwise anisotropic. Several computational methods have been developed to permit the reconstruction of the three-dimensional velocity distributions from the two-dimensional images [95]. When present, the anisotropy of the distribution can provide insights concerning the symmetry of the orbital from which the electron was removed.

The kinematics leading to image formation are such that the energy resolution is highest for slow-moving electrons [94]. Hence, the best resolution is achieved by tuning the detachment laser to a photon energy that is not much above the threshold for the channel that is being examined (referred to as slow-electron VMI (SEVI)). This is nicely illustrated by Leon et al. [95], who used photodetachment of Bi^- to demonstrate how the resolution improves (down to $1.2\,cm^{-1}$) as the kinetic energy imparted to the electron is reduced from 165.5 to $5.2\,cm^{-1}$.

Factors other than the image resolution limit the energy resolution in studies of molecular anions. In general, anions are rather fragile species. They are easily destroyed in laser ablation sources if the carrier gas pressure is too high. In many cases, the low pressures imposed by the anion instability result in poor cooling. The resolution of the SEVI technique is then compromised by the large number of internal energy states of the anion that are populated. Electrospray ionization has also been used to generate anions for SEVI measurements. This is a versatile source, but it usually produces anions under conditions that are at or above ambient temperatures. The strategy to solve this source temperature problem has been to accumulate the anions in ion traps and subject them to buffer gas cooling by low-pressure He. The trap electrodes can be cooled to temperatures as low as 4.4 K. After a period of accumulation and cooling, the anion packet is injected into the SEVI spectrometer (see Figure 1 of Reference [95]). Wang and coworkers have examined UOs [11, 97, 98], fluorides [99–101], and chlorides [102, 103] using the SEVI technique. As an example, Figure 1.10 shows the data for electron detachment from UF_5^- [101]. The structure present in this spectrum corresponds to the vibrational levels of UF_5. This figure illustrates the advantages of ion-trap cooling and the use of near-threshold photon energies.

1.3.7 Action Spectroscopy

In the present context, action spectroscopy refers to schemes where photoexcitation is detected by observing a molecular fragmentation event. Through mass spectrometric detection of the fragments, action spectroscopy is a powerful tool for probing molecular ions that can only be produced at low number densities. For uranyl-containing species, a particularly successful series of gas-phase action spectroscopy experiments has been carried out using the free electron laser (FELIX) that is currently located at Radbound University in the Netherlands [10, 44–48, 104, 105]. This facility is capable of

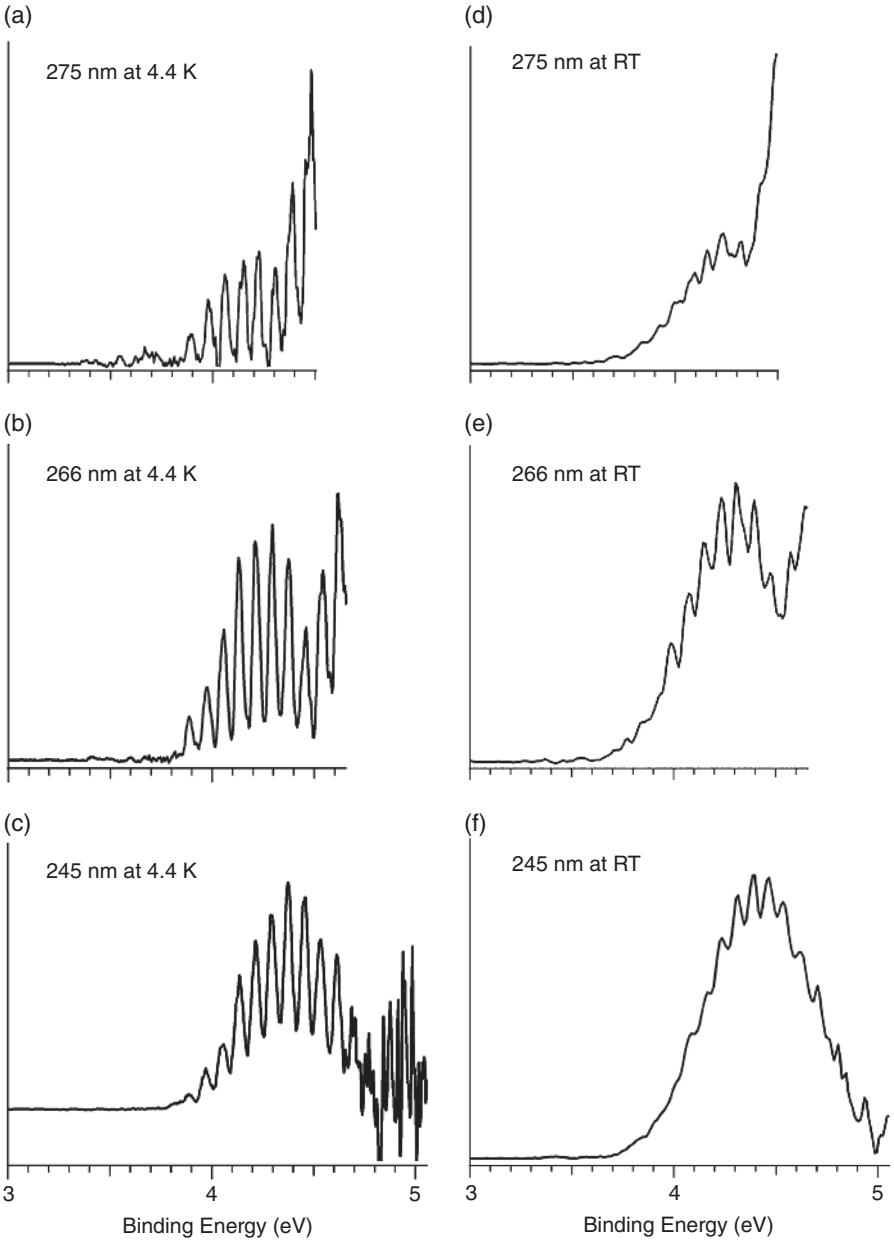

Figure 1.10 Photoelectron spectra of UF_5^- at an ion-trap temperature of 4.4 K (left), compared to those taken at room temperature (right) at (a) and (d) 275 nm (4.508 eV), (b) and (e) 266 nm (4.661 eV), and (c) and (f) 245 nm (5.061 eV). (Reproduced with permission from Dau, P.D., Liu, H.-T., Huang, D.-L., and Wang, L.-S. (2012) Note: Photoelectron spectroscopy of cold UF_5^-. *Journal of Chemical Physics*, **137**, 116101/1–116101/2.)

producing intense tunable radiation throughout the infrared region of the spectrum. For this experiment, various $(UO_2^{2+})L_n$ complexes (where L is a ligand or solvent molecule) have been generated in the gas phase by means of electrospray ionization. Uranyl nitrate solutions have proved to be suitable sources for UO_2^{2+}. The initial studies involved complexes of the uranyl ion with acetone and acetonitrile [48]. The complexes were accumulated in a hexapole trap and then injected into a Fourier transform ion cyclotron resonance mass spectrometer (FT-ICR-MS). A tailored frequency sweep of the ICR-MS was used to eject all ions except the species of interest. Once isolated, the ions were irradiated by intense IR pulses from the free electron laser. If the IR was resonant with a vibrational transition, a high-order multiphoton absorption process was triggered. The energy imparted by this event was sufficient to cause fragmentation of the parent ion. For example, the $(UO_2^{2+})(acetone)_4$ complex fragmented to $(UO_2^{2+})(acetone)_3$ + acetone when vibrational transitions in the range of 900–1800 cm^{-1} were excited. The FT-ICR-MS was used to characterize the fragmentation, and the relative IR absorption strengths were determined from the dissociation yields. Although fragmentation is induced by multiphoton processes, it has been shown that the absorption of the first photon controls the fragmentation. Hence, the data obtained are equivalent to conventional IR absorption spectra. The spectra reported to date have a resolution on the order of 15–20 cm^{-1}. This is sufficient to discern trends in the ion-ligand interactions. For the acetone and acetonitrile complexes, Groenewold et al. [48] clearly observed the effects of electron donation from the ligand on the uranyl asymmetric stretch. Over the past decade, complexes of uranyl with acetone [47, 48], acetonitrile [47, 48], water [47], ammonia [47] simple alcohols [46, 47], nitrate [45, 104], and the chelating ligand TMOGA [10] have been investigated.

The FELIX facility has yielded excellent spectroscopic data, but the need to carry out the measurements using this unique instrument is a significant practical limitation. Action spectroscopy using commercial laser sources at shorter wavelengths (below 3.5 μm) has been a productive endeavor for many years. The possibility of working at longer wavelengths in a typical university laboratory has been realized through improvements in the design of optical parametric oscillators (OPOs) and the availability of new materials for difference frequency down-conversion. The intensities from these systems are sufficient for robust excitation of single-photon transitions, and low-order multiphoton transitions may also be observed. However, the table-top laser systems are not powerful enough to drive the high-order multiphoton processes that are exploited in the FELIX experiments.

Duncan and coworkers have used IR action spectroscopy to study uranium oxide and uranium carbonyl cations [24, 42, 43, 106]. A pulsed laser ablation source was used to generate these species. Mass selection of the target ion and identification of the photofragments was accomplished using a reflectron time-of-flight mass spectrometer. The reflectron consists of two flight tubes and an electrostatic mirror. The latter reflects the ions back along a direction that is 5° away from the incident path. Duncan and coworkers installed a set of deflection electrodes in the first flight tube. These electrodes are used to mass-select the ions that are allowed into the mirror. Within the mirror, at the turning region of the ion trajectories, the ions are excited by the IR laser beam. The second limb of the reflectron then provides a time-of-flight mass analysis of the products.

Ricks et al. [42, 43] used this technique to examine the IR spectra of $U^+(CO)_n$ and $UO_2^+(CO)_m$ complexes with values of $n \leq 10$ and $m \leq 7$. They excited the CO stretch

modes of all complexes and the asymmetric stretch mode of the UO_2^+ moiety. The resulting fragmentation patterns showed that the $U^+(CO)_8$ and $UO_2^+(CO)_5$ complexes were particularly stable, indicative of the species with the highest coordination numbers. These results were in accordance with the predictions of DFT calculations. Ricks et al. [24] also examined the UO_4^+ and UO_6^+ ions. These are exotic species in that U is not expected to exhibit an oxidation state greater than six. However, a stable ion such as UO_2^+ can readily bind additional O_2 molecules under the low-temperature conditions of a free-jet expansion. Spectroscopic measurements for these oxide ions were complicated by the fact that IR excitation of the bare ions did not produce a measureable degree of fragmentation. Consequently, action spectra were obtained using a rare-gas atom tagging technique [24]. The ablation source was operated under conditions that generated the $UO_4^+Ar_2$ and $UO_6^+Ar_2$ van der Waals complexes, and the IR transitions were detected by observing the loss of one Ar atom. Interestingly, the complexes that started with just one Ar atom did not dissociate. The central assumption of the tagging method is that the van der Waals interactions will not significantly perturb the properties of the molecule (similar to the assumption made for cryogenic rare-gas matrix isolation experiments). Ricks et al. [24] were able to show that UO_4^+ was a charge transfer complex of the form $(UO_2^{2+})(O_2^-)$, while the second O_2 unit of UO_6^+ is weakly bound to the UO_4^+ core.

Pillai, Duncan, and coworkers [106] have also used their reflectron mass spectrometer to observe direct photodissociation of complexes consisting of benzene molecules bound to U^+, UO^+, and UO_2^+. Mass-selected clusters were photofragmented by the third harmonic from an Nd/YAG laser (355 nm). For $U^+(C_6H_6)$, they observed the fragments U^+, $U^+(C_4H_2)$, and $U^+(C_2H_2)$, showing that ligand decomposition was an important decay channel. The other clusters investigated, $U^+(C_6H_6)_n$, n = 2,3, $UO^+(C_6H_6)$, and $UO_2^+(C_6H_6)$, all exhibited simple intact loss of one C_6H_6 unit. Pillai et al. [106] noted that these trends were consistent with other studies of the relative gas-phase reactivities of U^+, UO^+, and UO_2^+.

1.3.8 Bond Energies and Reactivities from Mass Spectrometry

The spectroscopic techniques described in the preceding sections provide accurate information concerning the bonding mechanisms, electronic structure, equilibrium geometries, and vibrational modes of actinide-containing molecules. Basic thermodynamic information can be derived from these data via the application of the theorems of statistical mechanics. Another thermodynamic property, the ionization energy (IE), can be measured accurately using spectroscopic methods. However, bond energies and relative reactivities are not readily extracted from spectroscopic measurements alone.

Some of the earliest studies of actinides in the gas phase were carried out using classical mass spectrometry techniques. Measurements of ionization energies were made using thermal vaporization of the actinide compound, followed by electron impact ionization [107–110]. This method gave useful estimates of the energies, but, when high temperatures were needed for vaporization, the values could be compromised by the presence of thermally excited molecules that lowered the appearance potentials. Other thermodynamic properties were deduced from analyses of the equilibrium distributions of various species in the vapor phase, generated over a range of temperatures. Electron impact ionization mass spectrometry was used to characterize relative concentrations [13–15, 26–28, 30, 110–114]. Second and third law models were then used to extract the enthalpies and bond energies. Much of this work was recently reviewed for actinide oxides by Kovacs et al. [115].

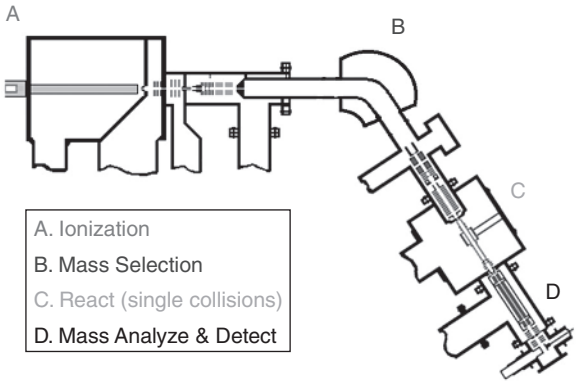

Figure 1.11 Guided ion-beam apparatus for studies of dissociative and reactive collisions with controlled collision energies. See text for details.

Bond dissociation energies for ionic species ($AB^+ \rightarrow A + B^+$) can be determined with good accuracy using collision-induced dissociation (CID) techniques. Armentrout and coworkers [25, 29, 116] have applied guided ion-beam CID to a wide range of metal-containing ions, including Th and U species. An example of the instrumentation used for CID measurements is shown in Figure 1.11. The two differentially pumped vacuum chambers shown on the left-hand side of this schematic are used for ion generation and ion-beam formation. Armentrout and coworkers have used laser ablation and a variety of discharge methods to generate gas-phase ions. In the next chambers, marked as region B in the figure, the ions are accelerated and mass-resolved using a magnetic sector mass spectrometer. After mass selection, the ion velocities are adjusted to the desired value, and they are injected into a collision cell (region C in Figure 1.11). The pressure of the inert collision gas (e.g., Ar or Xe) is chosen to yield single-collision events. Finally, the fragments are characterized using a quadrupole mass spectrometer (region D). One of the first applications of this technique to actinides was the study of UO^+ and UO_2^+ bond dissociation energies by Armentrout and Beauchamp [116]. The error ranges were on the order of 0.4 eV for bond energies of 8.0 and 7.7 eV. Note that the bond dissociation energy for a neutral molecule (D_0(A-B)) can be derived from a value for $D_0(A - B^+)$ by the IEs for AB and B, using the thermodynamic cycle $D_0(A - B) = D_0(A - B^+) + IE(AB) - IE(B)$.

The apparatus shown in Figure 1.11 has also been used in extensive studies of reactive collisions. Drawing on a recent example, Figure 1.12 shows data for the collisions between Th^+ and CD_4. Here, it can be seen that the lowest energy channel is the ejection of D_2 to form Th^+CD_2. Several other channels open at collision energies close to 2 eV. In this same study, Cox et al. [14] used Th^+CH_4 + Xe CID to measure the $Th^+CH_4 \rightarrow Th^+ + CH_4$ dissociation energy.

Other MS techniques have been used to investigate actinide species that include transuranic (Np-Es) and radiologically hazardous (Pa) materials. Gibson, Marçalo, and coworkers have developed the specialized facilities needed for these experiments [8, 12, 117]. Initially, Gibson and coworkers used laser ablation as the means to generate gas-phase ions. The ablation products were allowed to react with a reagent at low pressures (near single-collision conditions), and the products were analyzed by means of a TOF-MS. This technique was termed laser ablation with prompt reaction and detection

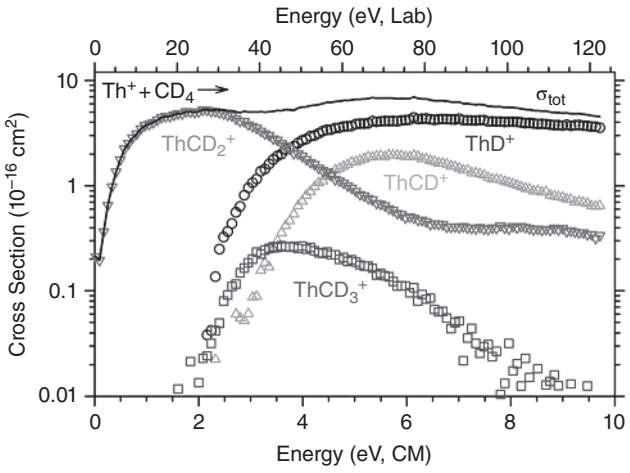

Figure 1.12 Cross sections for the reaction between Th^+ and CD_4 as a function of energy in the center of mass (lower *x* axis) and lab (upper *x* axis) frames of reference. (Reproduced with permission from Cox, R.M., Armentrout, P.B., and de Jong, W.A. (2015) Activation of CH_4 by Th^+ as studied by guided ion-beam mass spectrometry and quantum chemistry. *Inorganic Chemistry*, **54**, 3584–3599.) (*See insert for color representation of the figure*.)

(LAPRD) [118,119]. Bond dissociation and ionization energies have been obtained by a bracketing approach. As charge exchange processes of the kind $A^+ + B \rightarrow A + B^+$ do not have barriers, this method works well for determination of the first IE. Bond dissociation energies are more difficult to determine by bracketing studies. Consider a reaction of the form $MO^+ + OR \rightarrow MO_2^+ + R$. If the reaction is observed, it is evident that the O-MO^+ bond energy exceeds that of O-R. However, as there may be a barrier to the reaction, a negative result does not necessarily imply that the O-R bond energy exceeds that of O-MO^+. Reliable results can be obtained by combining the bracketing data with the predictions of electronic structure calculations.

Prior to the LAPRD studies of actinides, Fourier transform ion cyclotron resonance (FT-ICR) MS had been used to examine the reactions of Th^+ and U^+ [8]. Marçalo, Gibson, and coworkers [117] used similar instruments to examine the IEs, bond dissociation energies, and reaction pathways of many radiologically active actinides. In these experiments, ions are exposed to charge exchange or reaction partners within the ion trap. MS/MS double resonance techniques can then be used to observe the time-dependent loss of parent ions and the growth of charged product species. In favorable cases, reaction rate constants and branching ratios can be determined. Quadrupole ion-trap (QIT) MS provides another versatile technique for studying gas-phase actinide ion chemistry. Gibson and coworkers have had considerable success using a commercial QIT-MS with ESI [10, 13, 34–41, 120–123]. This system has been configured for work with radiologically active species, but it has also provided valuable new results for both Th and U compounds. As for the ICR system, the QIT can be programmed to trap selected ions, excite them, permit the addition of collision partners, and mass-analyze the charged reaction products. A notable example of the work with this system is provided by a recent study of the oxo exchange reactions between AnO_2^+ and H_2O for An = Pa and U [39]. $Pa^{16}O_2^+$ and $U^{16}O_2^+$ ions were generated by ESI of methanol/ethanol

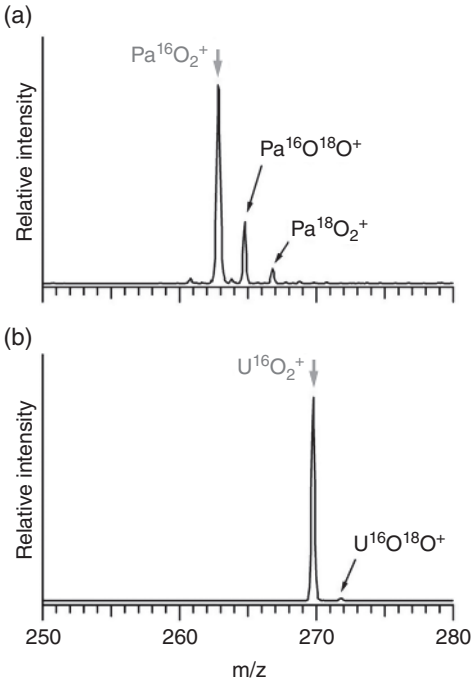

Figure 1.13 Mass spectra acquired after 0.5 s exposure to a constant $H^{18}O$ pressure for (a) $Pa^{16}O^{2+}$ and (b) $U^{16}O^{2+}$. Exchange of the first and second O is apparent for PaO^{2+}, whereas only very minor exchange of one O, is observed for UO^{2+}.

solutions. These ions were reacted with $H_2{}^{18}O$ in the QIT, and the results are shown in Figure 1.13. Here, it is immediately apparent that the oxo exchange with $PaO_2{}^+$ is much faster than the exchange with $UO_2{}^+$. The intermediate for this exchange is the bis-hydroxo species $AnO(OH)_2{}^+$, and it was suggested that it is the relative stability of this ion that controls the reaction rate. To test the stability of the $PaO_3H_2{}^+$ intermediate, this ion was trapped and exposed to a low pressure of acetonitrile. It had been established that ligated water could be replaced by the more strongly basic acetonitrile ligand, but that the bond strength was not sufficient for replacement of a hydroxyl group. This experiment confirmed that most of the $PaO_3H_2{}^+$ in the trap was of the bis-hydroxo form. The same measurements for $UO_3H_2{}^+$ showed facile replacement of the H_2O ligand. Further probes of the ion stabilities were carried out using CID. The interpretation of the MS/MS results were confirmed by electronic structure calculations that also provided structural information for the intermediates [124].

1.4 Considerations for Characterizing Actinide-Containing Molecules in the Gas Phase by Ab Initio Methods

In addition to the usual considerations of the electron correlation method and basis set, quantum chemical calculations on actinide-containing molecules present a number of additional difficulties that are somewhat reminiscent of the transition metals. The

actinides can exist in a number of oxidation states and have nearly degenerate 5f, 6d, 7s, and 7p orbitals. This leads to a high density of electronic states and often strong multideterminantal character even in their electronic ground states. This is particularly true for free radical actinide molecules, which can involve open 5f, 6d, and 7s shells. In addition, since the 6s and 6p orbitals have very similar radial extents as the 5f, these electrons must also be treated as valence along with the 5f, 6d, and 7s, leading to a large number of electrons to be treated even in frozen-core calculations, for example, already 14 for just the U atom. These same characteristics that make the electron correlation problem difficult also put strong demands on the underlying 1-particle basis set since a given valence set needs to represent orbitals from the 6s out to the 7p with occupied angular momenta ranging from s to f. Of course, for these heavy elements, the treatment of relativistic effects, both spin-orbit and particularly scalar, is mandatory even for a qualitative description.

1.4.1 Electron Correlation Methods

Among the ab initio methods commonly used for actinide species, DFT has played a major role due to its relatively modest computational cost and good accuracy. In regards to spectroscopy, it has been most widely used to provide quality estimates of structures and harmonic vibrational frequencies. Most studies have used the B3LYP hybrid exchange-correlation functional [125, 126], although generalized gradient approximation (GGA) functionals such as PW91 [127] and PBE [128] have also been utilized in the literature. Besides its relatively low computational cost, another advantage of DFT methods is the general availability of analytical gradients and even analytical hessians, which greatly facilitates the efficient calculation of minima, transition states, and harmonic frequencies. The main drawback of DFT methods, however, particularly in regard to predicting spectroscopic properties, is the lack of a route for systematic improvement of the results. Thus, it is critical to attempt an assessment of the accuracy of the calculated quantities of interest by carrying out analogous calculations on very similar species or carrying out high-accuracy benchmark calculations.

Currently the most accurate spectroscopic properties obtainable from ab initio methods are afforded, at least in principle, by wavefunction-based methods since they can be systematically improved toward the exact solution of a particular relativistic Hamiltonian. As in molecules not involving heavy elements, the coupled cluster singles and doubles with perturbative triples method, CCSD(T) [129], is still one of the main methods of choice for high accuracy. Its computational cost is much higher than DFT (approximately N^7 vs. N^4 where N is a measure of the system size), but it can still be applied to actinide molecules containing up to about 10 non-hydrogen atoms using modern computational resources. Of course, CCSD(T) can only be utilized for molecules where the wavefunction is well described by the Hartree–Fock determinant. This can quickly become problematic as the number of unpaired electrons, particularly in the open 5f shell, increases, which can make lower oxidation states particularly difficult. The successive removal of F from UF_6 provides an excellent example. The electron configuration on U for the formal oxidation state varies from $5f^0 7s^0$ in UF_6 to $5f^3 7s^0$ in UF_3 to $5f^3 7s^2$ in UF [99]. None of these species has nominally more than three electrons distributed in the 5f shell, but this still leads to significant multideterminantal character for the smaller systems UF_3, UF_2, and UF due to the near-degeneracy of the available spatial components of the 5f orbitals. Curiously, in these cases, this does not lead to large T_1 diagnostics for the previous three molecules (all are ≤0.03), but it does strongly

present itself in terms of symmetry-breaking problems and instabilities in the calculation of numerical derivatives for harmonic frequencies due to the many close-lying states. In part, this is a typical example related to the expression among computational chemists of "smaller is harder" that applies as well to calculations on undercoordinated transition metal compounds, for example, transition metal diatomics. It is worth noting here as well that since CCSD(T) is based on a single HF determinant, it is generally only applicable to electronic ground states or to excited states of differing spin multiplicities (in the absence of spin-orbit coupling).

For the situation where the wavefunction is not dominated by a single determinant, there are several multireference methods that have found widespread use for actinide spectroscopy. Probably the most ubiquitous in the actinide community is the complete active space self-consistent field (CASSCF) method [130] followed by second-order perturbation theory, that is, CASPT2 [131, 132]. In the CASSCF step, the orbitals must first be partitioned by the user into inactive, active, and external spaces. For the standard "full valence active space," the active space consists of all the molecular orbitals that can be constructed from the valence atomic orbitals of the atoms. The inactive space is defined as the lower-lying core orbitals, and the external space consists of the remaining unoccupied orbitals lying at higher energy above the active space. For example, for the N_2 molecule, the inactive space would correspond to the two doubly occupied MOs consisting of the two 1s core orbitals, and the full valence active space would consist of the eight MOs constructed from the 2s and 2p orbitals. All possible determinants of the desired space and spin symmetry are then constructed with the valence electrons (10 in the N_2 example) using the active space orbitals; that is, a full configuration interaction (FCI) calculation is carried out just within the active space orbitals, and the MO coefficients are also simultaneously optimized (generally including the inactive orbitals, which are constrained to be doubly occupied in all determinants).

A full valence CASSCF can be a fairly black-box procedure, particularly for molecules consisting of just main group elements, since the choice of active space orbitals can often be done in an automated, unambiguous manner. Unfortunately for most actinide molecules, the total number of valence molecular orbitals can become prohibitively large, particularly if both the 5f and 6d shells are deemed important (which is often the case). In particular, the number of determinants involved in the CAS has a factorial dependence on the number of active electrons and active space size, which can quickly become prohibitively expensive. Hence, some truncation of the active space is often necessary, which relies on a fair amount of chemical intuition and testing to ensure that important near-degeneracy effects are recovered in a balanced manner. As a rule of thumb, all orbitals should be included that are involved in a bond-breaking process or low-lying electronic states of interest, particularly including those that can interact strongly with the ground state. For example in the previous work by Gagliardi and co-workers [133] on oxides of Pa, for PaO it was possible to distribute nine electrons into 16 active orbitals, which consisted of the 7s, 6d, and 5f orbitals of Pa and the 2p orbitals of O. Not surprisingly, extending this same strategy to PaO_2 was found to be too demanding, and the active space was truncated by omitting the two lowest energy π_g bonding and corresponding antibonding orbitals, as well as one additional σ_g^* antibonding orbital. This yielded a nine electrons in 14 orbitals (9/14) CASSCF. Small molecules involving multiple actinide atoms are even more challenging as evidenced by the work of Roos et al. on actinide dimers [134]. On the basis of several trial studies, an active space for U_2 was reduced from the full valence 12 electrons in 26 orbitals space

(7s, 6d 5f) to 6 electrons in 20 orbitals. This was deemed sufficient near equilibrium but lacked sufficient flexibility for full potential curves. More complicated electron/orbital partitioning schemes can also be carried out that restrict the allowed excitations between subsets of orbitals. These methods are referred to as restricted active space [135] (RAS) or generalized active space [136] (GAS) approaches and can lead to a much smaller number of determinants (or CSFs) in the expansion of the wavefunction.

Just a CASSCF calculation alone, however, does not yield quantitative results since it mostly recovers just near-degeneracy effects, that is, non-dynamical electron correlation. Additional electron correlation, in particular dynamical correlation, can be recovered in a subsequent multiconfigurational second-order perturbation theory calculation with a reference function given by the CASSCF wavefunction. This method has been shown to yield reliable accuracy for actinide systems, although it can suffer from the "intruder state" problem which can cause serious convergence issues. These can generally be mitigated by a redefinition of the active space (adding more orbitals) or through appropriate level shifts. A computationally more expensive alternative to CASPT2 that can also use CASSCF as a reference function is the multireference configuration interaction (MRCI) method [137]. Unlike CASPT2, it is not size extensive, but this can be accounted for in an approximate manner via a multireference Davidson correction (MRCI + Q) [138]. Table 1.1 demonstrates the intricacies of assessing the accuracy of these methods for the $^6L_{11/2} \leftarrow {}^4I_{9/2}$ atomic excitation energy of the U^+ atom using a CASSCF of five electrons in 13 orbitals (5f, 6d, 7s) [139]. Spin-orbit coupling was included via the state interacting approach as discussed below. At the CASSCF level of theory, the wrong ground state is obtained by over 4000 cm^{-1}, while CASPT2 yields the correct ground state although it overestimates the experimental excitation energy (289 cm^{-1}) by about 850 cm^{-1}. Both MRCI and MRCI + Q yield the wrong ground state, although the effect of the + Q correction is very large, increasing the excitation energy relative to MRCI by nearly 1100 cm^{-1} and leaving the MRCI + Q result 971 cm^{-1} below the experimental value. Upon including the 5s, 5p, and 5d electrons into the correlation space at the CASPT2 level, however, the excitation energy is further increased compared to the valence correlated result by nearly 1100 cm^{-1}. This yields a CASPT2 excitation energy much larger than experiment (by 1921 cm^{-1}), but if this core-valence correlation correction is applied to the MRCI + Q result, excellent agreement with experiment is achieved. Unfortunately, this level of calculation becomes much too computationally demanding even for a study of the UF diatomic.

Table 1.1 Errors with respect to experiment (cm^{-1}) at the extrapolated complete basis set limit for the $^6L_{11/2} \leftarrow {}^4I_{9/2}$ transition of U^+. The 60-electron PP of Dolg and Cao [140] was used throughout.

Method	Valence correlation	Valence +5s5p5d[a]
CASSCF	−4573	—
CASPT2	+849	+1921
MRCI	−2058	−989[a]
MRCI + Q	−971	+115[a]

a Core correlation effect taken from the CASPT2 calculations.

As an alternative to the CASSCF/CASPT2 and MRCI methods, multireference coupled cluster theory has also been used in accurate calculations involving actinides. The most successful of these is the Fock space implementation, that is, FS-CCSD [141]. Its advantage is that the full electronic spectrum can be computed in a single calculation with a computational cost similar to standard CCSD. One of its main practical limitations, however, is that the desired open-shell state(s) must be within two electrons of a closed-shell reference determinant. Starting from this correlated reference state, denoted sector (0,0), an orbital active space or model (*P*) space is chosen in which to either add *n* electrons, sector (0,*n*), or remove *m* electrons, sector (*m*,0), and the correlation energy is solved at each step. The electronic spectrum of a molecule containing one or two electrons added to the unoccupied *P* space involves calculating sectors (0,1) and (0,2), respectively, while the spectrum for the molecule with one to two fewer electrons than the reference involves removing these electrons from the occupied space, that is, sectors (1,0) and (2,0). The electronic spectrum of the reference molecule itself can also be obtained by calculating sector (1,1). By its construction, FS-CCSD takes into account the multireference character of a state but is limited to just single and double excitations. In some cases, convergence issues are experienced in standard FS-CCSD due to intruder states, and this led to the development of the intermediate Hamiltonian (IH-) FS-CCSD method [142], where the *P* space is itself divided into two subspaces: a primary space and a buffer space. For example, Infante et al. [143] used the IH-FS-CCSD method to study the electronic states of UO_2 and UO_2^+. The UO_2^{2+} molecule was used as the closed-shell reference state, while UO_2^+ and UO_2 involved solving for sectors (0,1) and (0,2), respectively. The main model space consisted of the 7*s*, two of the five 6*d*, and six of the seven 5*f* orbitals of U.

1.4.2 Relativistic Effects

As noted earlier, the incorporation of effects due to relativity is essential in any calculation containing actinide atoms. There are roughly two strategies in use in regards to actinide calculations. In one case, a spin-free, scalar relativistic Hamiltonian is first employed to generate orbitals and perhaps also a basis of correlated electronic states, with spin-orbit coupling (SOC) then being introduced after the fact. In the second option, scalar and spin-orbit relativistic effects are included together from the beginning in either full four-component (positron and electron states) or two-component (only electron states) treatments. Both have their advantages and disadvantages in terms of their ease of interpretation, computational cost, and overall attainable accuracy. Scalar relativistic Hamiltonians in common use for actinide chemistry include the all-electron Douglas–Kroll–Hess [144, 145] (DKH) and exact two-component (X2C) Hamiltonians [146], as well as relativistic effective core potentials (RECPs) or pseudopotentials (PPs) [5]. Mostly commonly, the second-order DKH Hamiltonian (DKH2) is used, but recently it has been shown that DKH3 has a non-negligible effect even on energy differences and geometries compared to DKH2 if high accuracy is desired. The X2C approach is essentially analogous to infinite-order DKH, but is not as readily available as DKH. The PP approach has been very successful in actinide applications, generally yielding results in very good agreement with comparable all-electron treatments. The most accurate PPs for actinides subsume only 60 or 68 electrons in the effective potential, leaving at least the 5d, 6s, 6p, 6d, 5f, and 7s electrons explicitly in the valence space.

The first strategy of the above approaches to SOC has seen the widest application use in actinide chemistry, and in most cases this employs a state interacting approach [147, 148] where spin-orbit coupling is introduced via degenerate perturbation theory. In the first stage of these calculations, a set of electronic states is computed in the absence of SOC using a scalar-only relativistic Hamiltonian ($\hat{H}_{el}$). The final spin-orbit eigenstates are then obtained by explicitly constructing and diagonalizing $\hat{H}_{el} + \hat{H}_{SO}$ in a basis of these electronic states, which are eigenfunctions of $\hat{H}_{el}$. The results, of course, can be very sensitive to the number of basis states included as well as the level of theory used to compute them. Since the accuracy of the off-diagonal SO matrix elements is generally less sensitive to the level of theory than the spin-free electronic state separations themselves, this method easily allows for combining different sources for diagonal and off-diagonal elements of $\hat{H}_{el} + \hat{H}_{SO}$. One advantage of this approach is that the final SO eigenstates can be easily interpreted in terms of the contributions from electronic states of well-defined spin multiplicities (the basis states). In typical applications to actinide molecules, a set of scalar-only electronic states of various spin multiplicities are first computed using the CASPT2 method, and the SO matrix elements between them are obtained at the CASSCF level of theory with two-electron contributions to the SOC terms approximately obtained via the atomic mean-field integral (AMFI) [149] approximation. For example, in recent calculations of the low-lying electronic states of the UFO molecule to assist in the interpretation of the photoelectron spectrum of UFO^-, Roy et al. [100] utilized the all-electron second-order Douglas–Kroll–Hess (DKH2) scalar relativistic Hamiltonian with the CASPT2 method to compute up to 40 doublet and 40 quartet states with SO matrix elements determined by CASSCF. In this same work, a relativistic pseudopotential (PP) was also employed for both the zeroth-order CASPT2 states and CASSCF SO matrix elements, with both methods (DKH2 and PP) yielding a very consistent set of UFO electronic state separations and UFO^- vertical detachment energies.

A different strategy is presented by the SO-MRCI method, whereby the orbitals are determined in a scalar-only HF, CASSCF, or MCSCF (multiconfiguration self-consistent field) calculation, after which a single and double excitation SO-MRCISD calculation is carried out in conjunction with a PP-based SO operator employing double group symmetry [150]. This approach is very effective at recovering important SO effects, even for nominally closed-shell ground states where the state interacting approach can be less effective, but the resulting CI expansions grow very rapidly with system size. For instance, for the UO^+ molecule, Pitzer and coworkers [151] correlated 13 electrons in an MCSCF active space that included 10 orbitals, resulting in a SO-MRCI in a triple-zeta basis set with 33 million spin eigenfunctions. Extending the correlation treatment to also include the 3σ and 4σ orbitals formed from the U6pσ and O2pσ atomic orbitals increased the size of the resulting CI to a prohibitive 96 million CSFs. It should be noted that as in the state interacting approach, the resulting accuracy can be limited when the orbitals are strongly affected by SOC.

In terms of relativistic calculations with scalar relativity and SOC treated on the same footing, full four-component (4-c) calculations utilizing the Dirac–Coulomb (DC) or Dirac–Coulomb–Breit (DCB) Hamiltonians [152] in MRCI or CCSD(T) calculations [153, 154] are the gold standard, but this can be prohibitively expensive for many molecular calculations. Alternatively, the small and large components of the 4-c wavefunction can be decoupled, with the small component discarded, leading to so-called two-component (2-c) Hamiltonians. For all-electron wavefunction-based methods, the

two-component version of the X2C Hamiltonian [146] has been used extensively for calculations involving actinides, while the zeroth-order regular approximation [155] (ZORA) has been used for 2-c DFT. In the 2c-X2C approach the two-electron spin-same-orbit and spin-other-orbit corrections to SOC are obtained by either AMFIs or the molecular mean-field approach [156]. It is also possible to accurately use some PPs and their associated one-electron SO parameters, for example, the newer Stuttgart–Cologne small-core PPs [140, 157], in variational 2-c calculations, and these have also seen considerable use.

1.4.3 Basis Sets

Even with sophisticated treatments of electron correlation and relativity, the overall accuracy can still be strongly dependent on the quality of the one-particle basis set used to describe the molecular orbitals or spinors. This is just as true for PP-based calculations as it is for all-electron cases. Particularly for the accurate prediction of relative energies, such as bond dissociation enthalpies, being able to approach or extrapolate to the complete basis set (CBS) limit in a reliable, systematic manner is very valuable to minimize basis set incompleteness errors. The design and optimization of basis sets for actinide elements are challenging in themselves, as addressed in a recent review [158]. They must be able to describe electron correlation effects for electrons in the semi-core 6s and 6p orbitals up through the valence 7s in conjunction with either an all-electron or PP relativistic Hamiltonian. They must also be flexible enough to describe a large number of oxidation states and low-lying electronic states of the actinide atom. In order to provide angular correlation of the 5f electrons, already g-type functions are necessary and thus should be included even in a polarized valence double-zeta (VDZ) basis set. Relative energetics approaching chemical accuracy (1–3 kcal/mol) must also include expanding the correlation space to at least the 5d electrons, which requires further extensions of standard valence basis sets. With the exception of the Slater-type basis sets found in the ADF program [159] and used most often in relativistic DFT calculations, basis sets for actinides are constructed with Gaussian-type functions.

For use in all-electron, correlated calculations on actinides, there are three families of basis sets now in common use, the correlation consistent basis sets of Dyall [160] for use in fully relativistic four-component calculations (dyall.vnz), the atomic natural orbital (ANO) basis sets of Roos et al. [161] (ANO-RCC) for use with the DKH2 scalar relativistic Hamiltonian, and the correlation consistent basis sets of Peterson and coworkers [162, 163] constructed with the DKH3 Hamiltonian (cc-pV*n*Z-DK3). Each of these choices include basis sets ranging from small valence DZ up to quadruple-zeta (QZ) quality, with the Dyall and Peterson sets including extensions for 5s5p5d correlation. Both of the latter family of sets have the advantage of being amenable to standard CBS extrapolation techniques for the HF and correlation energies [164]. In regards to actinide DZ basis sets, the SARC sets of Pantazis and Neese [165] have been particularly designed for use in DFT calculations using the DKH2 and ZORA scalar relativistic Hamiltonians.

Gaussian basis sets constructed for use with relativistic PPs or ECPs include the correlation consistent cc-pVDZ and cc-pVTZ sets of Pitzer and coworkers [166] for use with the 68-electron PPs of Christiansen et al. [167], as well as the DZ quality basis sets originally accompanying the Stuttgart quasirelativistic 60-electron PPs of Küchle et al. [168] (the latter combination is also referred to as SDD in the literature) and the QZ set

also subsequently developed for the latter PP [169]. In addition to the QZ-quality basis sets accompanying the new energy-consistent multiconfigurational Dirac–Hartree–Fock (MCDHF)-adjusted (60-electron) PPs of Dolg and coworkers [140, 157] (Ac–U), Peterson [162] has recently reported correlation consistent basis sets from DZ through QZ (cc-pVnZ-PP), together with core correlation sets (cc-pwCVnZ-PP), for use with these latter PPs for Th through U. Since these sets are very similar in construction to the all-electron DKH3 correlation consistent sets noted above, these two families of basis sets have been used in CCSD(T) calculations to demonstrate the high attainable accuracy of these PPs [162, 170].

The most common quantum chemistry programs used for actinide calculations (typical methods used given in parentheses) include MOLCAS [171] (CASSCF and SO-CASPT2), MOLPRO [172] (single-reference coupled cluster, CASSCF, SO-CASPT2, SO-MRCI), DIRAC [173] (two- and four-component relativistic HF, DFT, MRCI, and coupled cluster), and GAUSSIAN [174] (DFT).

1.5 Computational Strategies for Accurate Thermodynamics of Gas-Phase Actinide Molecules

Given the challenges of experimentally determining gas phase bond enthalpies and heats of formation of actinide-containing molecules, computational quantum chemistry can play a very important role in accurately determining the thermodynamic stability of actinide species, particularly those whose short lifetime or radioactivity makes laboratory studies difficult. As is now well known in light main group chemistry, the reliable prediction of thermochemical properties to chemical accuracy (1 kcal/mol) by ab initio methods requires a systematic treatment of both electron correlation and basis set incompleteness errors [175]. Typically, this implies using at least two correlation consistent basis sets of increasing size, generally at least triple- and quadruple-zeta, with extrapolation to the CBS limit using high levels of electron correlation such as CCSD(T). Corrections for outer-core electron correlation and relativistic effects are then included together with accurate harmonic frequencies for zero-point vibrations and thermal corrections. This collection of calculations is the minimal basis for most composite thermochemistry calculations in common use for lighter elements, such as FPA [176], Wn [177], HEAT [178], ccCA [179], and FPD [175,180]. This is not to say that accurate results cannot be obtained by simply choosing one particular method and basis set, although by its very nature this implies some fortuitous, and perhaps significant, cancellation of errors that can lead to unexpected results.

Recently one of the present authors has extended the composite FPD thermochemistry methodology to molecules containing actinide elements [162]. Versions based on both relativistic PPs and the all-electron DKH3 Hamiltonian were investigated, with the all-electron approach yielding the highest average accuracy. Utilizing geometries optimized at the frozen-core DKH3-CCSD(T)/cc-pVTZ-DK3 level of theory, the following procedure was adopted:

- The Hartree–Fock energy was computed with cc-pwCV*n*Z-DK3 [162] and aug-cc-pcWV*n*Z-DK [181–183] basis sets on the actinide and lighter elements, respectively,

with n = T and Q. These energies were extrapolated to the HF CBS limit by [184] $E_n = E_{CBS} + A(n+1)e^{-6.57\sqrt{n}}$ (n = 3 for TZ and n = 4 for QZ).

- The CCSD(T) correlation energy with valence (6s6p5f6d7s) and outer-core (5s5p5d) electrons of the actinide atom together with the valence and outer-core electrons of the lighter elements were calculated with cc-pwCV*n*Z-DK3 and aug-cc-pwCV*n*Z-DK [185] basis sets with n = T and Q. The correlation energy was extrapolated to the CBS limit via [186] $E_n = E_{CBS} + \frac{B}{(n+1/2)^4}$. In practice, this step was obtained by carrying out separate valence and core correlation calculations in order to assess the impact of the core correlation. Ideally, a CBS limit for valence correlation would be combined with a smaller basis set core correlation calculation for the core-valence correlation effect, but it was found that the effect of 5s5p5d correlation was very slowly convergent with basis set and required extrapolation.
- Contributions due to SOC were calculated using completely uncontracted cc-pVDZ-DK3 and aug-cc-pVDZ-DK basis sets with the X2C Hamiltonian [146], which includes atomic-mean-field two-electron spin-same-orbit corrections. Two-component, frozen-core coupled cluster calculations were then carried out, either CCSD(T) or FS-CCSD on the basis of how well the wavefunction was dominated by a single determinant. The contribution of the Gaunt term of the Breit interaction was evaluated in all-electron X2C or 4-c calculations at the Dirac–Hartree–Fock level. Atomic SOC corrections for light elements were generally obtained by *J*-averaging of the experimental term energies.
- The leading quantum electrodynamic (QED) contributions from the Lamb shift, that is, the self-energy and vacuum polarization, were obtained via a model potential approach proposed by Pyykkö and Zhao [187]. This local potential was added to the one-electron DKH3 Hamiltonian in frozen-core CCSD(T)/cc-pwCVDZ-DK3/aug-cc-pVDZ-DK calculations and compared to the analogous calculation without this modification.
- Harmonic vibrational frequencies calculated at the CCSD(T)/cc-pVDZ-DK3/aug-cc-pVDZ-DK level of theory were utilized for both the zero-point vibrational corrections and thermal corrections, the latter being obtained from standard ideal gas partition functions.

Table 1.2 shows representative results [162] using the above scheme for the atomization energy of ThO_2 and the first two bond dissociation enthalpies (BDEs) of UF_6 (all relative to 298 K). As explicitly shown in Reference [162], the CBS limit of Table 1.2 for the ThO_2 atomization energy was larger than the QZ result by nearly 4 kcal/mol, while the UF_6 BDEs were only larger by a few tenths of a kcal/mol. In all three cases, the effect of correlating the 5s5p5d electrons of Th and U is non-negligible, affecting the energetics by 2.0 to 2.7 kcal/mol. It is worth mentioning that this is not all due to the 5d electrons; 5s5p correlation accounted for up to 1 kcal/mol of these values. Obviously, the effects due to SOC are essential to include, particularly for the ThO_2 atomization energy, due to the large SO of Th atom, and the bond enthalpy of UF_5, since both UF_5 and UF_4 are open-shell species. The calculated effects due to QED were small but certainly not negligible for the atomization energy of ThO_2. In all cases, the final enthalpies are well within the experimental uncertainties.

Table 1.2 Summary of composite FPD thermochemistry contributions and comparison to experiment (in kcal/mol).

Process	CBS[TQ]	ΔCV[a]	ΔSO[b]	ΔQED	ΔZPE	ΔH(0)	ΔH(298)	ΔH(expt)
$ThO_2 \rightarrow Th + 2O$	374.5	2.7	−8.4	+0.8	−2.4	366.8	369.0	367.8 ± 3.2[c]
$UF_6 \rightarrow UF_5 + F$	80.7	−2.1	−3.0	−0.4	−1.8	73.4	73.9	71.0 ± 2.9[d] 75.3 ± 4[c]
$UF_5 \rightarrow UF_4 + F$	104.8	−2.0	−6.4	−0.4	−1.6	94.3	95.7	98.0 ± 3.6[d] 92.5 ± 5.3[c]

a CCSD(T)/CBS[wTQ] with 5s5p5d correlation on Th and U as well as 1s correlation of O and F.
b Includes small contributions due to the Gaunt interaction.
c From the experimental heats of formation; see Reference [162] for details.
d Reference [188].

The FPD values discussed above are based on the CCSD(T) method, which is, of course, not an exact treatment of electron correlation. Going beyond CCSD(T) involves carrying out CCSDT [189, 190] and CCSDTQ [191] or CCSDT(Q) [192] calculations, which are nearly prohibitively expensive for actinide-containing molecules given the large intrinsic basis set sizes and number of valence electrons to correlate. It is feasible, however, for select diatomic molecules, such as ThC^+ and ThO. In the latter case, a CCSDTQ/cc-pVDZ-DK3(Th)/aug-cc-pVDZ-DK(O) calculation involved about 4.3 billion configurations [193]. The resulting impacts on the dissociation energies of ThC^+ and ThO, which were calculated in support of guided ion-beam experiments [193], were largest for the CCSDT – CCSD(T) correction, −1.2 kcal/mol for both molecules, while the effects of quadruple excitations, CCSDTQ – CCSDT, were just +0.3 and +0.06 kcal/mol for ThC^+ and ThO, respectively. Given the apparently fast convergence of the coupled cluster sequence for these molecules, the final dissociation energies were estimated to be accurate to well under 1 kcal/mol.

A complication in accurately determining the BDEs of actinide molecules, although this occurs more generally in the calculation of heats of formation, is that the atoms are often much more difficult to treat with single determinant-based methods like CCSD(T) than their molecules. For instance, the ground electronic state of U has a valence electron configuration of $5f^36d^17s^2$, which is not very amenable to HF-based calculations. One route around this is to revert to an isodesmic reaction approach using molecules with well-known heats of formation, such as UF_6 [194]. This was recently used to good effect by Bross and Peterson [170] to determine the heats of formation for several U-containing molecules using a similar CCSD(T) FPD scheme as outlined above. As is well known from the ab initio thermochemistry of lighter molecules, the use of isodesmic reactions can also be accurately used to avoid carrying out high-level composite treatments such as FPD. Thanthiriwatte et al. [195] used isodesmic reactions to determine the BDEs of ThF_4, as well as its cations and anions. Using the frozen-core CCSD(T) method with the older 60 electron PP of Küchle et al. [168] on Th with the segmented contracted basis set of Cao and Dolg [169] together with the aug-cc-pVTZ set [181, 182] on F, their resulting dissociation energies were within the experimental error bars (around 3 kcal/mol) in most cases. They also carried out B3LYP calculations, which agreed well with CCSD(T) in these cases.

As mentioned earlier, DFT has been applied extensively in molecular actinide chemistry, and this includes the calculation of BDEs. Perhaps not surprisingly, its performance is mixed, partly because this method's accuracy is just as dependent on the accurate treatment of relativistic effects, particularly SOC, as wavefunction-based approaches, but also due to sensitivity in the choice of functional. For example, Peralta et al. [196] used the hybrid B3LYP and PBEh [197, 198] functionals together with the DKH3 Hamiltonian to calculate the BDEs of the series UF_n and UCl_n with n = 1–6. With their best treatment of SOC, which was a self-consistent treatment with approximate screened-nuclear two-electron SO contributions (SNSO), the agreement with experiment ranged from under 1 to 11 kcal/mol (ignoring the very poor agreement for UF and UCl, which was presumably due to the difficulties with atomic U as previously discussed). Their SNSO contributions seem to strongly underestimate the SOC effects on the BDEs in comparison to the X2C coupled cluster results of Reference [162]. Use of the latter values to correct the scalar results of Peralta et al. [196] improves the agreement with experiment for UF_6 (SOC correction of –3.2 kcal/mol compared to –0.3 kcal/mol) while moving the UF_5 result (SOC correction of –6.7 kcal/mol compared to –0.9 kcal/mol) strongly away from what was originally very good agreement. The choice of functional also had an impact in some cases, with differences of 9 and 10 kcal/mol for UF_4 and UCl_2, respectively, between B3LYP and PBEh. Armentrout and coworkers [14, 30, 193] have also used various DFT functionals in comparison to CCSD(T) using relativistic PPs in support of guided ion-beam mass spectrometry experiments. In calculations on $Th(CH_n)^+$ species (n = 1–4)[14], the average error with respect to experiment for all three functionals used (B3LYP, B3PW91 [125, 127], and BHandHLYP [174]) was about 8 kcal/mol compared to about 6.5 kcal/mol for their frozen-core CCSD(T) calculations with the cc-pVQZ-PP basis set [162] on Th (and cc-pVTZ on the light atoms). Individual variations among the different functionals were much larger, however, with BHandHLYP exhibiting the largest differences ranging up to nearly 24 kcal/mol for $ThCH^+$.

Of course, all of the above strategies can be used for other energy differences, such as ionization potentials and electron affinities. Table 1.3 shows FPD results for the IE of ThO [193], which is very accurately known from experiment, 152.2603(6) kcal/mol [199]. The agreement of the FPD composite approach with experiment is nearly perfect in this case. It is worth recognizing that the effect of SOC on the IE, +0.74 kcal/mol, is rather large considering that the ionization involves a removal of a 7s electron from the

Table 1.3 Summary of composite FPD calculations of the ionization energy of ThO (in kcal/mol).

CBS[TQ][a]	ΔCV[b]	ΔSO[c]	ΔQED[d]	ΔT[e]	ΔQ[f]	ΔZPE[g]	IE(0)	IE(expt)
150.92	+0.18	+0.74	–0.31	–0.02	+0.33	+0.08	152.29	152.2603

a CCSD(T)/CBS[TQ] within the frozen-core approximation (6s6p6d7s of Th, 2s2p of O correlated).
b CCSD(T)/CBS[wTQ] correlation effect of correlating the 5s5p5d electrons of Th and 1 s of O.
c X2C, 2c-CCSD(T) with uncontracted cc-pVDZ-DK3/aug-cc-pVDZ basis sets.
d DKH3-CCSD(T)/cc-pwCVDZ-DK3/aug-cc-pwCVDZ-DK with a QED model potential.
e CCSDT – CCSD(T) in cc-pVTZ-DK3/aug-cc-pVTZ-DK basis sets using DKH3.
f CCSDTQ – CCSDT in cc-pVDZ-DK3/aug-cc-pVDZ-DK basis sets using DKH3.
g Using DKH3-CCSD(T)/cc-pVDZ-DK3/aug-cc-pVDZ-DK harmonic frequencies.

closed-shell ThO molecule. This is consistent, however, with the uranium isodesmic reaction enthalpies of Bross and Peterson [170], where SOC contributions were on the order of 1 kcal/mol even though all species were formally closed-shell singlets.

As in isodesmic reactions, the calculation of ionization potentials or electron affinities can often benefit from cancellation of errors since the two species involved often have very similar electronic structures. As an example, Gagliardi and coworkers [200] applied both the SO-CASPT2 and X2C-CCSD(T) methods with basis sets of just valence TZ and DZ quality, respectively, to obtain ionization potentials for both AnO and AnO_2 species (An = Th, U, Np, Pu, Am, Cm). Their results compared very well with the experimental values determined by Marçalo and Gibson [201] by FTICR/MS. In addition, Gagliardi and coworkers [202] also have reviewed the performance of several wavefunction-based methods with DFT on ionization potentials and bond energies of actinide monoxides and dioxides, albeit with ANO-RCC basis sets of just TZ quality. Surprisingly, their results demonstrated very similar accuracy between several DFT functionals with either CASPT2 or CCSD(T); however, the experimental uncertainties used for comparison were often relatively large, that is, 3–17 kcal/mol.

1.6 Ab Initio Molecular Spectroscopy of Gas-Phase Actinide Compounds

In principle, the accurate ab initio calculation of spectroscopic properties could follow the same procedure as described above for ab initio thermochemistry, except that now many configurations need to be sampled on the potential energy surface (PES) rather than just at the global minimum and dissociation asymptote(s). The need for many energy evaluations, however, can turn a computationally expensive thermochemistry calculation into something intractable for an accurate spectroscopy study. This is particularly true for situations where multireference methods are required, which is nearly always the case for excited electronic states. Particularly in these cases, sampling configurations away from the PES minimum necessarily involves lowering the symmetry, which can greatly increase the computational cost. Of course, in cases where single determinant-based methods are appropriate, analytical derivative techniques can sometimes be used to obtain geometries and harmonic frequencies. This strategy has been used most extensively at the DFT level of theory for ground state actinide chemistry.

1.6.1 Pure Rotational and Ro-Vibrational Spectroscopy

As an example of using the FPD composite scheme for spectroscopic properties, Table 1.4 shows the CCSD(T) spectroscopic constants for the $^1\Sigma^+$ ground electronic state of ThO. The values were obtained by fitting seven energies distributed about the equilibrium geometry to polynomials in simple displacement coordinates, and the resulting derivatives were subjected to a Dunham analysis. The frozen-core (FC) calculations involved cc-pV*n*Z-DK3 (Th) and aug-cc-pV*n*Z-DK (O) basis sets (*n* = D–Q, denoted V*n*Z below) with the DKH3 scalar relativistic Hamiltonian. The core correlation calculations (CV) involved additional correlation of the 5s5p5d electrons of Th and the 1s electrons of O using cc-pwCV*n*Z-DK3 and aug-cc-pwCV*n*Z-DK basis sets (*n* = D-Q, denoted wC*n*Z

Table 1.4 Calculated CCSD(T) spectroscopic constants of $X^1\Sigma^+$ ThO compared to experiment.

	R_e (Å)	ω_e (cm^{-1})	$\omega_e x_e$ (cm^{-1})
Valence correlation			
VDZ	1.8671	859.37	2.16
VTZ	1.8524	883.58	2.30
VQZ	1.8488	887.03	2.25
CBS[TQ][a]	1.8471	888.80	2.22
ΔCV[b]			
wCVDZ	+0.0001	+3.21	-0.01
wCVTZ	−0.0037	+6.01	+0.03
wCVQZ	−0.0053	+7.12	+0.01
CBS[wTQ]	−0.0062	+7.77	+0.00
ΔSOC	−0.0001	+3.75	+0.04
Final values	1.8399	901.2	2.26
Experiment	1.840186[c]	895.77[d]	2.39[d]

a The FC CBS limits using the wCV*n*Z basis sets were 1.8462 Å, 889.70 cm^{-1}, and 2.22 cm^{-1} for R_e, ω_ε, and $\omega_e x_e$, respectively. These values were used in the final composite results.

b The wCV*n*Z basis sets were used in both frozen-core and core correlation calculations of the near-equilibrium potential energy function.

c Reference [70].

d Reference [16].

below). CBS extrapolations were carried out as outlined in the previous section. The SOC calculations utilized the two-component X2C Hamiltonian in relativistic CCSD(T) calculations with uncontracted cc-pVDZ-DK3 and aug-cc-pVDZ basis sets with spin-same-orbit two-electron contributions using the AMFI approximation.

As seen in Table 1.4, the final composite spectroscopic constants are in excellent agreement with experiment, with the bond length within 0.0003 Å and the harmonic frequency within ~5 cm^{-1}. Improvement of these final results would presumably require electron correlation beyond CCSD(T). The convergence with basis set is smooth and relatively rapid, with the VTZ results being with 0.005 Å and about 5 cm^{-1} from the FC CBS limits of R_e and ω_e. Correlation of the 5s5p5d electrons of Th is not an insignificant effect, although the bond length and harmonic frequency are lowered and raised, respectively, by just 0.006 and 7.8 cm^{-1}. As expected for this nominally closed-shell molecule, the effect of SOC is relatively minor.

Among actinide diatomic molecules, ThO is an anomaly in that its wavefunction is dominated by a single determinant. A more typical example is the UO molecule, which involves two close-lying electronic states, one correlating to U^{2+} in a $5f^37s$ configuration and another with U^{2+} in a $5f^27s^2$ configuration [18]. High-level spin-orbit MRCI calculations have been carried out by Pitzer and coworkers [151] on UO and UO^+ using TZ-quality basis sets and small-core relativistic PPs. These calculations aptly demonstrate how complicated such "simple" molecules can be. The ground state of UO was calculated to be an $\Omega = 4$ state (correlating to the $5f^37s$ configuration) consistent with

experiment with a bond length agreeing to within about 0.01 Å, which is to be expected with a basis set of this size. Earlier, Hirao and coworkers [203] also computed the spectroscopic properties of UO and UO^+ but at the DKH2-CASPT2 level of theory with an ANO-RCC-QZP basis set [161]. They also determined the ground state to be $\Omega = 4$ with 71% attributable to the ^{5}I state. Their calculated bond length and harmonic frequency were in excellent agreement with experiment, which might be partially attributed to the larger basis set used.

Beyond the examples of diatomic molecules, very few anharmonic force fields have been calculated for actinide polyatomic molecules, although anharmonic vibrational anharmonicity constants at the CCSD(T) level have been previously reported for both UO_2^{2+} and ThO_2 [204]. In regard to calculating harmonic frequencies of actinide molecules, Odoh and Schreckenbach [205] have demonstrated the importance of using small-core PPs compared to large-core ones (the latter with 5d in the core) in DFT calculations of UO_3 and UF_6. In particular, the small-core Stuttgart PPs yielded B3LYP equilibrium geometries and harmonic frequencies in good agreement with full four-component B3LYP calculations. In regard to the performance of different functionals, at least in the case of UF_6, B3LYP and PBE0 calculations yielded harmonic frequencies in better agreement with experiment compared to PBE, BPBE [125, 128], or BLYP [125, 126]. In one of the earliest applications of CASPT2 to actinide molecules, Gagliardi and Roos [206] found that in the case of several U(V) and U(VI) triatomics, CASPT2 gave much better agreement with experiment compared to B3LYP when VTZ basis sets were used; that is, the largest relative error for CASPT2 was just 4% in a basis with g-type functions, while it reached 10% for B3LYP.

While not strictly gas phase, there has been a particularly fruitful interplay between theory and experiment in the area of matrix isolation infrared spectroscopy [8]. Recent calculations of structures and harmonic frequencies have mostly been carried out using the combination of B3LYP with the Stuttgart 60-electron PP of Küchle et al. [168] and the VQZ basis set from Cao and Dolg [169]. One very interesting example is the linear CUO molecule, which was first observed [207] in a Ne matrix with an assignment assisted by calculated harmonic frequencies and isotope shifts at the scalar relativistic DFT level using the PW91 functional with a TZ Slater-type-orbital (STO) basis set. The ground state was assigned at that point as $^1\Sigma^+$, on the basis of the close correspondence of the DFT frequencies from that electronic state with experiment. The story became more interesting, however, when experiments in an Ar matrix were carried out, and the vibrational spectrum was very different as compared to that in neon [208]. Gas-phase DFT calculations [208] indicated that a low-lying $^3\Phi$ state had vibrational frequencies very similar to those observed for CUO in an Ar matrix. Hence, it was proposed that the more polarizable Ar directly interacted with the CUO molecule, inverting the order of these two states and resulting in a $^3\Phi$ ground state. This seemed confirmed by further experiments in a matrix consisting of 1% argon in neon [209]. More extensive ab initio calculations by Roos et al. [210] at the DKH2-CASPT2/ANO-RCC-QZP level of theory, however, seemed to put this interpretation strongly in doubt. In particular, their work placed the $^3\Phi$ state below the $^1\Sigma^+$, and the inclusion of SOC, which had not been done yet to that point, further stabilized the $\Omega = 2$ component of the $^3\Phi$ compared to the $\Omega = 0$ arising from the $^1\Sigma^+$. Thus, the $^3\Phi_2$ state was predicted to be the ground state of CUO with an equilibrium excitation energy to the $^1\Sigma^+$ of over 12 kcal/mol, which could not explain the experimental observations in the neon matrix.

The following year, however, Infante and Visscher [211] used both relativistic (scalar and SO) ZORA, as well as full four-component (4-c) Dirac-Coulomb-CCSD(T) and FS-CCSD, to investigate the two lowest electronic states of UCO. Their scalar-only ZORA results were consistent with the original calculations of Andrews et al., yielding a $^1\Sigma^+$ ground state, but the inclusion of SOC reversed the order of states, which contradicts the interpretation of the experiments. However, at the 4-c coupled cluster level, either CCSD(T) or FS-CCSD, the $^1\Sigma_0{}^+$ state was computed to lie lower than the $^3\Phi_2$ by about 13.9 kcal/mol. This agreed well with experiment in that several heavy noble gas atoms were required to reverse the ordering of states. More recently, Yang et al. [212] carried out PP-based SO-MRCI calculations on CUO and obtained results consistent with the coupled cluster values, albeit with a smaller excitation energy of just 3.9 kcal/mol.

1.6.2 Electronic Spectroscopy

One particular area in the gas phase spectroscopy of actinide molecules that ab initio electronic structure methods can very effectively contribute to is in the interpretation and prediction of their complicated electronic spectra. In recent years, the workhorse in this area has been the CASPT2 method using the state interacting approach for SOC effects. This method and general strategy has been effective for interpreting/predicting both absorption and emission spectra, as well as negative ion photodetachment spectra. The strength of the CASPT2 method, as mentioned earlier, is that it is amenable to any spin state. This differs from the IH-FS-CCSD method, which can handle at most two electrons outside a closed-shell reference state. There have been a few studies that have directly compared CASPT2 to multireference CCSD, but these have been complicated by the use of different basis sets, relativistic Hamiltonians, or numbers of correlated electrons. In their study on UO_2 and $UO_2{}^+$, Infante et al. [143] carried out a detailed comparison of CASPT2 and IH-FS-CCSD for the related atomic ions U^{5+} and U^{4+} using identical basis sets and 4-c relativistic Hamiltonians. A total of 52 electrons were correlated for U^{4+}; that is, a [Kr] core was used. A summary of some of their error statistics is given in Table 1.5 for the U^{4+} ion for electronic transitions ranging from 4,000 to 100,000 cm^{-1}.

As discussed in Reference [143], one disadvantage of the IH-FS-CCSD approach for U^{4+} is the use of orbitals from the highly charged U^{6+} system. The majority of the orbital relaxation is recovered from the single excitation amplitudes, but this is incomplete

Table 1.5 Mean unsigned errors (in cm^{-1}) with respect to experiment for the U^{4+} ion from Reference [143] using the universal basis set of Malli et al. [213].

Transition type	Experimental energy range (cm^{-1})	CASPT2 (DC[a])	CASPT2 (DCB[b])	IH-FSCCSD (DC[a])	IH-FSCCSD (DCB[b])
$5f^2$	<44,000	814	825	514	357
5f6d	<68,000	3,467	6,024	2,824	2,110
5f7s	<103,000	657	3,610	3,548	2,680

a 4-c Dirac–Coulomb Hamiltonian

b 4-c Dirac–Coulomb–Breit Hamiltonian

without higher excitation operators or a more expanded active space. The effects of this are observed in Table 5, where the errors in the excitation energies for IH-FS-CCSD involving the more diffuse 6d and 7s orbitals are much larger than those involving the 5f alone. Upon comparing CASPT2 (with an active space involving the 5f, 6d, and 7s orbitals) to IH-FS-CCSD with the DC Hamiltonian, a very similar average accuracy is seen for the $5f^2$ transitions, but larger and smaller errors are found with CASPT2 for 5f6d and 5f7s transitions, respectively. Interestingly, the average errors of CASPT2 increase strongly in the cases of the 5f6d and 5f7s transitions (transition energies typically overestimated) when the more complete DCB Hamiltonian is employed, while this Hamiltonian improves the agreement of IH-FS-CCSD on average for these same transitions (transition energies generally underestimated). Hence, some significant cancellation of errors seem to occur in the CASPT2 case, similar to the example of U^+ given above in Table 1.1. It is not clear, however, how this comparison would change if only the valence electrons were correlated. These challenges for an atomic system, however, do help underscore the difficulties involved in reliably computing accurate electronic spectra of molecular actinide species.

1.7 Summary and Outlook

The interplay between gas-phase experimental studies and computational models has been steadily advancing our understanding of actinide bonding and reactivity. On the experimental side, a variety of laser spectroscopic and ion-beam/ion-trap mass spectrometric techniques are now yielding a wealth of incisive new data. In parallel, relativistic quantum chemistry methods are providing critical insights that cannot be obtained from the experimental data alone. For example, the permanent electric dipole of a molecule encodes information regarding the ground state wavefunction, but the nuanced physical significance can only be recovered through comparisons with theory. Consider ThS, where the experimental values for the dipole moment and bond length are 4.58(10) D and 2.3436(7) Å, respectively [82]. A high-level theoretical calculation (multireference configuration interaction) predicts that the ground state is an admixture of 56% $Th^{2+}(7s^2)S^{2-}(3s^23p^6)$ with 17% $Th^+(7s^26d)S^-(3s^23p^5)$ [85]. Clearly, the dipole moment will be sensitive to the relative weights of these configurations, and the predicted dipole moment (4.2 D) is in reasonable agreement with the experimental data. This correlation, along with the reliable prediction of both the bond length and vibrational frequency, confirms the validity of the calculations. It is then of interest to ask how well does a single-reference DFT calculation perform for this multi-configurational ground state? For ThS, the answer is that the B3LYP scheme does remarkably well [82], giving results of comparable quality to MRCI. Further study of ThS and related molecules can be used to explore the underlying reasons for the success, and the situations that might lead to failure of the less rigorous models. Turning to an example where the 5*f* electrons are of importance, experimental and theoretical studies of UF and UF^+ show that the $5f^3$ configuration on the metal ion retains its atomic character in the molecule/molecular ion, with minimal participation in the covalent bonding [31, 139]. Significant challenges still exist for theory, however, when multi-determinantal wavefunctions are present, particularly when SOC is included. Previously reliable results have been obtained using CASPT2, but new developments at both ends of the accuracy scale need further

development, particularly for molecules containing transuranium elements. These future developments will need accurate gas-phase spectroscopic data in order to assess their ranges of applicability.

Thermodynamic properties derived from mass spectrometric methods are validating new composite theoretical models for bond dissociation energies, ionization energies, and heats of formation [170, 214]. Studies of gas-phase reactions indicate that actinide $f \rightarrow d$ electron promotion energies are important in determining reactivities [8]. The application of action spectroscopy techniques, in combination with theoretical modeling, is expanding our knowledge of ligand binding, coordination numbers, and the local environments of solvated actinide ions [10, 24, 42–44, 104, 105]. Trends are beginning to emerge from these studies, and the information needed for the development of truly predictive models is being assembled. For the immediate future, we anticipate that rigorous studies of isolated molecules will accelerate progress in our understanding of actinide chemistry, permitting a dramatic increase in the size and complexity of actinide systems that can be meaningfully explored by the methods of relativistic quantum chemistry.

Acknowledgments

Michael Heaven gratefully acknowledges support from the US Department of Energy (grant DE-FG02-01ER15153-12) for the actinide research carried out at Emory University. Kirk Peterson also gratefully acknowledges support from the US Department of Energy under grant DE-FG02-12ER16329.

References

1 Pyykkö, P. (2012) The physics behind chemistry and the periodic table. *Chemical Reviews (Washington, DC, U. S.)*, **112**, 371–384.
2 Pyykkö, P. (2012) Relativistic effects in chemistry: More common than you thought. *Annual Reviews of Physical Chemistry*, **63**, 45–64.
3 Schwerdtfeger, P. (2014) Relativity and chemical bonding. *Chemical Bond*, **1**, 383–404.
4 Pepper, M. and Bursten, B.E. (1991) The electronic structure of actinide-containing molecules: A challenge to applied quantum chemistry. *Chemical Reviews*, **91**, 719–741.
5 Dolg, M. and Cao, X. (2012) Relativistic pseudopotentials: Their development and scope of applications. *Chemical Reviews (Washington, DC, U. S.)*, **112**, 403–480.
6 Cao, X. and Dolg, M. (2011) Pseudopotentials and model potentials. *WIREs Comput. Mol. Sci.*, **1**, 200–210.
7 Heaven, M.C., Barker, B.J., and Antonov, I.O. (2014) Spectroscopy and structure of the simplest Actinide bonds. *Journal of Physical Chemistry A*, **118**, 10867–10881.
8 Heaven, M.C., Gibson, J.K., and Marçalo, J. (2010) Molecular spectroscopy and reactions of the actinides in the gas phase and cryogenic matrices, in *The Chemistry of the Actinide and Transactinide Elements*, L.R. Morss, N.M. Edelstein, and J. Fuger, Editors. Springer, Dordrecht, the Netherlands. pp. 4079–4156.
9 Heaven, M.C. (2006) Probing actinide electronic structure using fluorescence and multiphoton ionization spectroscopy. *Physical Chemistry Chemical Physics*, **8**, 4497–4509.

10 Gibson, J.K., Hu, H.-S., van Stipdonk, M.J., Berden, G., Oomens, J., and Li, J. (2015) Infrared multiphoton dissociation spectroscopy of a gas-phase complex of uranyl and 3-oxa-glutaramide: An extreme red-shift of the $[O=U=O]^{2+}$ asymmetric stretch. *Journal of Physical Chemistry A*, **119**, 3366–3374.

11 Li, W.-L., Su, J., Jian, T., Lopez, G.V., Hu, H.-S., Cao, G.-J., Li, J., and Wang, L.-S. (2014) Strong electron correlation in UO_2^-. A photoelectron spectroscopy and relativistic quantum chemistry study. *Journal of Chemical Physics*, **140**, 094306/1–094306/9.

12 Gibson, J.K., Haire, R.G., Marçalo, J., Santos, M., Leal, J.P., Pires de Matos, A., Tyagi, R., Mrozik, M.K., Pitzer, R.M., and Bursten, B.E. (2007) FTICR/MS studies of gas-phase actinide ion reactions: Fundamental chemical and physical properties of atomic and molecular actinide ions and neutrals. *European Physical Journal D*, **45**, 133–138.

13 Dau, P.D., Armentrout, P.B., Michelini, M.C., and Gibson, J.K. (2016) Activation of carbon dioxide by a terminal uranium-nitrogen bond in the gas-phase: A demonstration of the principle of microscopic reversibility. *Physical Chemistry Chemical Physics*, **18**, 7334–7340.

14 Cox, R.M., Armentrout, P.B., and de Jong, W.A. (2015) Activation of CH_4 by Th^+ as studied by guided ion beam mass spectrometry and quantum chemistry. *Inorganic Chemistry*, **54**, 3584–3599.

15 Armentrout, P.B. (2013) The power of accurate energetics (or thermochemistry: What is it good for?). *Journal of the American Society for Mass Spectrometry*, **24**, 173–185.

16 Edvinsson, G., Selin, L.E., and Aslund, N. (1965) Band spectrum of ThO. *Arkiv foer Fysik*, **30**, 283–319.

17 Gresh, D.N., Cossel, K.C., Zhou, Y., Ye, J., and Cornell, E.A. (2016) Broadband velocity modulation spectroscopy of ThF^+ for use in a measurement of the electron electric dipole moment. *Journal of Molecular Spectroscopy*, **319**, 1–9.

18 Kaledin, L.A., McCord, J.E., and Heaven, M.C. (1994) Laser spectroscopy of UO: Characterization and assignment of states in the 0- to 3-eV Range, with a comparison to the electronic structure of ThO. *Journal of Molecular Spectroscopy*, **164**, 27–65.

19 Holt, J., Neese, F.N., De Lucia, F.C., Medvedev, I., and Heaven, M.C. (2014) The submillimeter spectrum OF UO, in *69th International Symposium on Molecular Spectroscopy*. University of Illinois.

20 Kaledin, L.A., Kulikov, A.N., Kobylyanskii, A.I., Shenyavskaya, E.A., and Gurvich, L.V. (1987) Reciprocal arrangements of the groups of low-lying states of uranium monoxide molecules. *Zhurnal Fizicheskoi Khimii*, **61**, 1374–1376.

21 Kaledin, L.A., Shenyavskaya, E.A., and Gurvich, L.V. (1986) Electronic spectra of uranium monoxide molecules. *Zhurnal Fizicheskoi Khimii*, **60**, 1049–1050.

22 Cossel, K.C., Gresh, D.N., Sinclair, L.C., Coffey, T., Skripnikov, L.V., Petrov, A.N., Mosyagin, N.S., Titov, A.V., Field, R.W., Meyer, E.R., Cornell, E.A., and Ye, J. (2012) Broadband velocity modulation spectroscopy of HfF^+: Towards a measurement of the electron electric dipole moment. *Chemical Physics Letters*, **546**, 1–11.

23 Duncan, M.A. (2012) Invited review article: Laser vaporization cluster sources. *Review of Scientific Instruments*, **83**, 041101/1–041101/19.

24 Ricks, A.M., Gagliardi, L., and Duncan, M.A. (2011) Uranium oxo and superoxo cations revealed using infrared spectroscopy in the gas phase. *Journal of Physical Chemistry Letters*, **2**, 1662–1666.

25 Loh, S.K., Hales, D.A., Li, L., and Armentrout, P.B. (1989) Collision-induced dissociation of iron cluster ions (Fe_n^+) (n = 2 – 10) with xenon: Ionic and neutral iron binding energies. *Journal of Chemical Physics*, **90**, 5466–5485.

26 Lau, K.H. and Hildenbrand, D.L. (1982) Thermochemical properties of the gaseous lower valent fluorides of uranium. *Journal of Chemical Physics*, **76**, 2646–2652.

27 Lau, K.H. and Hildenbrand, D.L. (1984) Thermochemical studies of the gaseous uranium chlorides. *Journal of Chemical Physics*, **80**, 1312–1317.

28 Lau, K.H. and Hildenbrand, D.L. (1990) High-temperature equilibrium studies of the gaseous thorium chlorides. *Journal of Chemical Physics*, **92**, 6124–6130.

29 Armentrout, P.B. and Beauchamp, J.L. (1980) Reactions of U^+ and UO^+ ions with diatomic oxygen, carbon monoxide, carbon dioxide, carbon oxide sulfide, carbon disulfide and water-d2. *Chemical Physics*, **50**, 27–36.

30 Cox, R.M., Armentrout, P.B., and de Jong, W.A. (2016) Reactions of $Th^+ + H_2$, D_2, and HD studied by guided ion beam tandem mass spectrometry and quantum chemical calculations. *Journal of Physical Chemistry B*, **120**, 1601–1614.

31 Antonov, I.O. and Heaven, M.C. (2013) Spectroscopic and theoretical investigations of UF and UF^+. *Journal of Physical Chemistry A*, **117**, 9684–9694.

32 Merritt, J.M., Kaledin, A.L., Bondybey, V.E., and Heaven, M.C. (2008) The ionization energy of Be_2, and spectroscopic characterization of the $(1)^3\Sigma^+_u$, $(2)^3\Pi_g$, and $(3)^3\Pi_g$ states. *Physical Chemistry Chemical Physics*, **10**, 4006–4013.

33 Wang, L.-S. (2015) Perspective: Electrospray photoelectron spectroscopy: From multiply-charged anions to ultracold anions. *Journal of Chemical Physics*, **143**, 040901/1–040901/14.

34 Van Stipdonk, M.J., O'Malley, C., Plaviak, A., Martin, D., Pestok, J., Mihm, P.A., Hanley, C.G., Corcovilos, T.A., Gibson, J.K., and Bythell, B.J. (2016) Dissociation of gas-phase, doubly-charged uranyl-acetone complexes by collisional activation and infrared photodissociation. *International Journal of Mass Spectrometry*, **396**, 22–34.

35 Maurice, R., Renault, E., Gong, Y., Rutkowski, P.X., and Gibson, J.K. (2015) Synthesis and structures of plutonyl nitrate complexes: Is plutonium heptavalent in $PuO_3(NO_3)^{2-}$? *Inorganic Chemistry*, **54**, 2367–2373.

36 Lucena, A.F., Lourenco, C., Michelini, M.C., Rutkowski, P.X., Carretas, J.M., Zorz, N., Berthon, L., Dias, A., Conceicao Oliveira, M., Gibson, J.K., and Marçalo, J. (2015) Synthesis and hydrolysis of gas-phase lanthanide and actinide oxide nitrate complexes: A correspondence to trivalent metal ion redox potentials and ionization energies. *Physical Chemistry Chemical Physics*, **17**, 9942–9950.

37 Lucena, A.F., Carretas, J.M., Marçalo, J., Michelini, M.C., Gong, Y., and Gibson, J.K. (2015) Gas-phase reactions of molecular oxygen with uranyl(V) anionic complexes-synthesis and characterization of new superoxides of uranyl(VI). *Journal of Physical Chemistry A*, **119**, 3628–3635.

38 Gong, Y., de Jong, W.A., and Gibson, J.K. (2015) Gas phase uranyl activation: Formation of a uranium nitrosyl complex from uranyl azide. *Journal of the American Chemical Society*, **137**, 5911–5915.

39 Dau, P.D., Wilson, R.E., and Gibson, J.K. (2015) Elucidating protactinium hydrolysis: The relative stabilities of $PaO_2(H_2O)^+$ and $PaO(OH)_2^+$. *Inorganic Chemistry*, **54**, 7474–7480.

40 Dau, P.D. and Gibson, J.K. (2015) Halide abstraction from halogenated acetate ligands by actinyls: A competition between bond breaking and bond making. *Journal of Physical Chemistry A*, **119**, 3218–3224.

41 Dau, P.D., Carretas, J.M., Marçalo, J., Lukens, W.W., and Gibson, J.K. (2015) Oxidation of actinyl(V) complexes by the addition of nitrogen dioxide is revealed via the replacement of acetate by nitrite. *Inorganic Chemistry*, **54**, 8755–8760.

42 Ricks, A.M., Reed, Z.E., and Duncan, M.A. (2011) Infrared spectroscopy of mass-selected metal carbonyl cations. *Journal of Molecular Spectroscopy*, **266**, 63–74.

43 Ricks, A.M., Gagliardi, L., and Duncan, M.A. (2010) Infrared spectroscopy of extreme coordination: The carbonyls of U^+ and UO_2^+. *Journal of the American Chemical Society*, **132**, 15905–15907.

44 Groenewold, G.S., van Stipdonk, M.J., Oomens, J., de Jong, W.A., Gresham, G.L., and McIlwain, M.E. (2010) Vibrational spectra of discrete UO_2^{2+} halide complexes in the gas phase. *International Journal of Mass Spectrometry*, **297**, 67–75.

45 Groenewold, G.S., Oomens, J., de Jong, W.A., Gresham, G.L., McIlwain, M.E., and van Stipdonk, M.J. (2008) Vibrational spectroscopy of anionic nitrate complexes of UO_2^{2+} and Eu^{3+} isolated in the gas phase. *Physical Chemistry Chemical Physics*, **10**, 1192–1202.

46 Groenewold Gary, S., van Stipdonk Michael, J., de Jong Wibe, A., Oomens, J., Gresham Garold, L., McIlwain Michael, E., Gao, D., Siboulet, B., Visscher, L., Kullman, M., and Polfer, N. (2008) Infrared spectroscopy of dioxouranium(V) complexes with solvent molecules: Effect of reduction. *ChemPhysChem*, **9**, 1278–1285.

47 Groenewold Gary, S., Gianotto Anita, K., McIlwain Michael, E., Stipdonk Michael, J.V., Kullman, M., Moore David, T., Polfer, N., Oomens, J., Infante, I., Visscher, L., Siboulet, B., and Jong Wibe, A.D. (2008) Infrared spectroscopy of discrete uranyl anion complexes. *Journal of Physical Chemistry B*, **112**, 508–521.

48 Groenewold, G.S., Gianotto, A.K., Cossel, K.C., van Stipdonk, M.J., Moore, D.T., Polfer, N., Oomens, J., de Jong, W.A., and Visscher, L. (2006) Vibrational spectroscopy of mass-selected $[UO_2(ligand)_n]^{2+}$ complexes in the gas phase: Comparison with theory. *Journal of the American Chemical Society*, **128**, 4802–4813.

49 Gasner, E.L. and Frlec, B. (1968) Raman spectrum of neptunium hexafluoride. *Journal of Chemical Physics*, **49**, 5135–5137.

50 Beitz, J.V., Williams, C.W., and Carnall, W.T. (1982) Fluorescence studies of neptunium and plutonium hexafluoride vapors. *Journal of Chemical Physics*, **76**, 2756–2757.

51 Person, W.B., Kim, K.C., Campbell, G.M., and Dewey, H.J. (1986) Absolute intensities of infrared-active fundamentals and combination bands of gaseous plutonium hexafluoride and neptunium hexafluoride. *Journal of Chemical Physics*, **85**, 5524–5528.

52 Kim, K.C. and Mulford, R.N. (1989) The combination bands ($\nu_1 + \nu_3$, $\nu_2 + \nu_3$) and overtone band ($3\nu_3$) of neptunium hexafluoride. *Chemical Physics Letters*, **159**, 327–330.

53 Kim, K.C. and Mulford, R.N. (1990) Vibrational properties of actinide (uranium, neptunium, plutonium, americium) hexafluoride molecules. *Journal of Molecular Structure THEOCHEM*, **66**, 293–299.

54 Mulford, R.N., Dewey, H.J., and Barefield, J.E., II, (1991) Fluorescence and absorption spectroscopy of the near-infrared vibronic transitions in matrix-isolated neptunium fluoride (NpF_6). *Journal of Chemical Physics*, **94**, 4790–4796.

55 Mulford, R.N. and Kim, K.C. (1996) Measurement and analysis of the Fourier transform spectra of the ν_3 fundamental and $\nu_1 + \nu_3$ combination of NpF_6. *Journal of Molecular Spectroscopy*, **176**, 369–374.

56 Aldridge, J.P., Brock, E.G., Filip, H., Flicker, H., Fox, K., Galbraith, H.W., Holland, R.F., Kim, K.C., Krohn, B.J., and et al. (1985) Measurement and analysis of the

infrared-active stretching fundamental (ν_3) of uranium hexafluoride. *Journal of Chemical Physics*, **83**, 34–48.

57 McDowell, R.S., Asprey, L.B., and Paine, R.T. (1974) Vibrational spectrum and force field of uranium hexafluoride. *Journal of Chemical Physics*, **61**, 3571–3580.

58 McDowell, R.S., Reisfeld, M.J., Nereson, N.G., Krohn, B.J., and Patterson, C.W. (1985) The $\nu_1 + \nu_3$ combination band of uranium-238 hexafluoride. *Journal of Molecular Spectroscopy*, **113**, 243–249.

59 Edvinsson, G., Bornstedt, A.V., and Nylen, P. (1968) Rotational analysis for a perturbed $^1\Pi$ state in thorium oxide. *Arkiv foer Fysik*, **38**, 193–218.

60 Edvinsson, G. and Jonsson, J. (1991) *On the K-X and M-X Band Systems of Thorium Monoxide (ThO)*. Dep. Phys.,Univ. Stockholm, Stockholm, Sweden. 30 pp.

61 Edvinsson, G. and Lagerqvist, A. (1984) Rotational analysis of yellow and near infrared bands in thorium(II) oxide. *Physica Scripta*, **30**, 309–320.

62 Edvinsson, G. and Lagerqvist, A. (1985) Rotational analysis of two red band systems in the thorium oxide (ThO) spectrum. *Physica Scripta*, **32**, 602–610.

63 Edvinsson, G. and Lagerqvist, A. (1985) A low-lying $\Omega = 2$ state in the thorium monoxide (ThO) molecule. *Journal of Molecular Spectroscopy*, **113**, 93–104.

64 Edvinsson, G. and Lagerqvist, A. (1987) Rotational analysis of some violet and green bands in the thorium oxide (ThO) spectrum. *Journal of Molecular Spectroscopy*, **122**, 428–439.

65 Edvinsson, G. and Lagerqvist, A. (1988) Two band systems of thorium oxide (ThO) in the near ultraviolet. *Journal of Molecular Spectroscopy*, **128**, 117–125.

66 Edvinsson, G. and Lagerqvist, A. (1990) Two new band systems in thorium oxide (ThO). *Physica Scripta*, **41**, 316–320.

67 Edvinsson, G. and Selin, L.E. (1964) Band spectrum of thorium oxide. *Physics Letters*, **9**, 238–239.

68 Dewberry, C.T., Etchison, K.C., and Cooke, S.A. (2007) The pure rotational spectrum of the actinide-containing compound thorium monoxide. *Physical Chemistry Chemical Physics*, **9**, 4895–4897.

69 Dewberry, C.T., Etchison, K.C., Grubbs, G.S., Powoski, R.A., Serafin, M.M., Peebles, S.A., and Cooke, S.A. (2007) Oxygen-17 hyperfine structures in the pure rotational spectra of SrO, SnO, BaO, HfO and ThO. *Physical Chemistry Chemical Physics*, **9**, 5897–5901.

70 Long, B.E., Novick, S.E., and Cooke, S.A. (2014) Measurement of the J = 1-0 pure rotational transition in excited vibrational states of $X^1\Sigma$ thorium (II) oxide, ThO. *Journal of Molecular Spectroscopy*, **302**, 1–2.

71 Allen, G.C., Baerends, E.J., Vernooijs, P., Dyke, J.M., Ellis, A.M., Feher, M., and Morris, A. (1988) High-temperature photoelectron spectroscopy: A study of uranium and uranium oxides (UO and UO_2). *Journal of Chemical Physics*, **89**, 5363–5372.

72 Maartensson, N., Malmquist, P.A., Svensson, S., and Johansson, B. (1984) The electron spectrum of uranium hexafluoride recorded in the gas phase. *Journal of Chemical Physics*, **80**, 5458–5464.

73 Beeching, L.J., Dyke, J.M., Morris, A., and Ogden, J.S. (2001) Study of the electronic structure of the actinide tetrabromides $ThBr_4$ and UBr_4 using ultraviolet photoelectron spectroscopy and density functional calculations. *Journal of Chemical Physics*, **114**, 9832–9839.

74 Boerrigter, P.M., Snijders, J.G., and Dyke, J.M. (1988) A reassignment of the gas-phase photoelectron spectra of the actinide tetrahalides uranium tetrafluoride, uranium tetrachloride, thorium tetrafluoride and thorium tetrachloride by relativistic Hartree-Fock-Slater calculations. *Journal of Electron Spectroscopy and Related Phenomena*, **46**, 43–53.

75 Dyke, J.M., Fayad, N.K., Morris, A., Trickle, I.R., and Allen, G.C. (1980) A study of the electronic structure of the actinide tetrahalides uranium tetrafluoride, thorium tetrafluoride, uranium tetrachloride, and thorium tetrachloride using vacuum ultraviolet photoelectron spectroscopy and SCF-Xα scattered wave calculations. *Journal of Chemical Physics*, **72**, 3822–3827.

76 Gagliardi, L., Skylaris, C.-K., Willetts, A., Dyke, J.M., and Barone, V. (2000) A density functional study of thorium tetrahalides. *Physical Chemistry Chemical Physics*, **2**, 3111–3114.

77 Sinclair, L.C., Cossel, K.C., Coffey, T., Ye, J., and Cornell, E.A. (2011) Frequency comb velocity-modulation spectroscopy. *Physical Review Letters*, **107**, 093002/1–093002/4.

78 Stephenson Serena, K. and Saykally Richard, J. (2005) Velocity modulation spectroscopy of ions. *Chemical Reviews*, **105**, 3220–3234.

79 Demtröder, W. (2008) *Laser Spectroscopy: Vol. 2: Experimental Techniques*. 4 ed. Vol. 2. Berlin: Springer-Verlag.

80 Stowe, M.C., Thorpe, M.J., Pe'er, A., Ye, J., Stalnaker, J.E., Gerginov, V., and Diddams, S.A. (2008) Direct frequency comb spectroscopy. *Advances in Atomic, Molecular, and Optical Physics*, **55**, 1–60.

81 Wang, F., Le, A., Steimle, T.C., and Heaven, M.C. (2011) Communication: The permanent electric dipole moment of thorium monoxide, ThO. *Journal of Chemical Physics*, **134**, 031102/1–031102/3.

82 Le, A., Heaven, M.C., and Steimle, T.C. (2014) The permanent electric dipole moment of thorium sulfide, ThS. *Journal of Chemical Physics*, **140**, 024307/1–024307/5.

83 Heaven, M.C., Goncharov, V., Steimle, T.C., Ma, T., and Linton, C. (2006) The permanent electric dipole moments and magnetic g factors of uranium monoxide. *Journal of Chemical Physics*, **125**, 204314/1–204314/11.

84 Linton, C., Adam, A.G., and Steimle, T.C. (2014) Stark and Zeeman effect in the [18.6]3.5 – X(1)4.5 transition of uranium monofluoride, UF. *Journal of Chemical Physics*, **140**, 214305/1–214305/7.

85 Bartlett, J.H., Antonov, I.O., and Heaven, M.C. (2013) Spectroscopic and Theoretical Investigations of ThS and ThS^+. *Journal of Physical Chemistry A*, **117**, 12042–12048.

86 Barker, B.J., Antonov, I.O., Heaven, M.C., and Peterson, K.A. (2012) Spectroscopic investigations of ThF and ThF^+. *Journal of Chemical Physics*, **136**, 104305/1–104305/9.

87 Steimle, T., Kokkin, D.L., Muscarella, S., and Ma, T. (2015) Detection of thorium dimer via two-dimensional fluorescence spectroscopy. *Journal of Physical Chemistry A*, **119**, 9281–9285.

88 Kokkin, D.L., Steimle, T.C., and DeMille, D. (2014) Branching ratios and radiative lifetimes of the U, L, and I states of thorium oxide. *Physical Review A Atomic, Molecular, and Optical Physics*, **90**, 062503/1–062503/10.

89 Steimle, T.C., Zhang, R., and Heaven, M.C. (2015) The pure rotational spectrum of thorium monosulfide, ThS. *Chemical Physics Letters*, **639**, 304–306.

90 Schlag, E.W. (1998) *ZEKE Spectroscopy*. 256 pp.

91 Linton, C., Simard, B., Loock, H.P., Wallin, S., Rothschopf, G.K., Gunion, R.F., Morse, M.D., and Armentrout, P.B. (1999) Rydberg and pulsed field ionization-zero electron kinetic energy spectra of YO. *Journal of Chemical Physics*, **111**, 5017–5026.

92 Yang, D.-S. (2011) High-resolution electron spectroscopy of gas-phase metal-aromatic complexes. *Journal of Physical Chemistry Letters*, **2**, 25–33.

93 Goncharov, V., Kaledin, L.A., and Heaven, M.C. (2006) Probing the electronic structure of UO^+ with high-resolution photoelectron spectroscopy. *Journal of Chemical Physics*, **125**, 133202/1–133202/8.

94 Neumark, D.M. (2008) Slow electron velocity-map imaging of negative ions: Applications to spectroscopy and dynamics. *Journal of Physical Chemistry A*, **112**, 13287–13301.

95 Leon, I., Yang, Z., Liu, H.-T., and Wang, L.-S. (2014) The design and construction of a high-resolution velocity-map imaging apparatus for photoelectron spectroscopy studies of size-selected clusters. *Review of Scientific Instruments*, **85**, 083106/1–083106/12.

96 Kim, J.B., Weichman, M.L., and Neumark, D.M. (2015) Low-lying states of FeO and FeO^- by slow photoelectron spectroscopy. *Molecular Physics*, Ahead of Print.

97 Su, J., Li, W.-L., Lopez, G.V., Jian, T., Cao, G.-J., Li, W.-L., Schwarz, W.H.E., Wang, L.-S., and Li, J. (2016) Probing the electronic structure and chemical bonding of mono-uranium oxides with different oxidation states: UO_x^- and UO_x (x = 3–5). *Journal of Physical Chemistry A*, **120**, 1084–1096.

98 Czekner, J., Lopez, G.V., and Wang, L.-S. (2014) High resolution photoelectron imaging of UO^- and UO_2^- and the low-lying electronic states and vibrational frequencies of UO and UO_2. *Journal of Chemical Physics*, **141**, 244302/1–244302/8.

99 Li, W.-L., Hu, H.-S., Jian, T., Lopez, G.V., Su, J., Li, J., and Wang, L.-S. (2013) Probing the electronic structures of low oxidation-state uranium fluoride molecules UF_x^- (x = 2–4). *Journal of Chemical Physics*, **139**, 244303/1–244303/8.

100 Roy, S.K., Jian, T., Lopez, G.V., Li, W.-L., Su, J., Bross, D.H., Peterson, K.A., Wang, L.-S., and Li, J. (2016) A combined photoelectron spectroscopy and relativistic ab initio studies of the electronic structures of UFO^- and UFO. *Journal of Chemical Physics*, **144**, 084309/1–084309/11.

101 Dau, P.D., Liu, H.-T., Huang, D.-L., and Wang, L.-S. (2012) Note: Photoelectron spectroscopy of cold UF_5^-. *Journal of Chemical Physics*, **137**, 116101/1–116101/2.

102 Su, J., Dau, P.D., Liu, H.-T., Huang, D.-L., Wei, F., Schwarz, W.H.E., Li, J., and Wang, L.-S. (2015) Photoelectron spectroscopy and theoretical studies of gaseous uranium hexachlorides in different oxidation states: UCl_6^{q-} (q = 0–2). *Journal of Chemical Physics*, **142**, 134308/1–134308/13.

103 Su, J., Dau, P.D., Xu, C.-F., Huang, D.-L., Liu, H.-T., Wei, F., Wang, L.-S., and Li, J. (2013) A joint photoelectron spectroscopy and theoretical study on the electronic structure of UCl_5^- and UCl_5. *Chemistry – Asian Journal*, **8**, 2489–2496.

104 Groenewold, G.S., van Stipdonk, M.J., Oomens, J., de Jong, W.A., and McIlwain, M.E. (2011) The gas-phase bis-uranyl nitrate complex $[(UO_2)_2(NO_3)_5]^-$: Infrared spectrum and structure. *International Journal of Mass Spectrometry*, **308**, 175–180.

105 Groenewold, G.S., de Jong, W.A., Oomens, J., and van Stipdonk, M.J. (2010) Variable denticity in carboxylate binding to the uranyl coordination complexes. *Journal of the American Society for Mass Spectrometry*, **21**, 719–727.

106 Pillai, E.D., Molek, K.S., and Duncan, M.A. (2005) Growth and photodissociation of $U^+(C_6H_6)_n$ (n = 1–3) and $UO_m^+(C_6H_6)$ (m = 1,2) complexes. *Chemical Physics Letters*, **405**, 247–251.

107 Rauh, E.G. and Ackermann, R.J. (1975) First ionization potentials of neptunium and neptunium monoxide. *Journal of Chemical Physics*, **62**, 1584.

108 Rauh, E.G. and Ackermann, R.J. (1974) First ionization potentials of some refractory oxide vapors. *Journal of Chemical Physics*, **60**, 1396–1400.

109 Ackermann, R.J. and Rauh, E.G. (1973) Preparation and characterization of the metastable monoxides of thorium and uranium. *Journal of Inorganic and Nuclear Chemistry*, **35**, 3787–3794.

110 Hildenbrand, D.L. (1977) Thermochemistry of gaseous uranium pentafluoride and uranium tetrafluoride. *Journal of Chemical Physics*, **66**, 4788–4794.

111 Hildenbrand, D.L. (1988) Equilibrium measurements as a source of entropies and molecular constant information. *Pure and Applied Chemistry*, **60**, 303–307.

112 Hildenbrand, D.L. and Lau, K.H. (1991) Redetermination of the thermochemistry of gaseous uranium fluorides (UF_5, UF_2, and UF). *Journal of Chemical Physics*, **94**, 1420–1425.

113 Kleinschmidt, P.D. and Hildenbrand, D.L. (1979) Thermodynamics of the dimerization of gaseous uranium(V) fluoride. *Journal of Chemical Physics*, **71**, 196–201.

114 Lau, K.H. and Hildenbrand, D.L. (1987) Thermochemistry of the gaseous uranium bromides UBr through UBr_5. *Journal of Chemical Physics*, **86**, 2949–2954.

115 Kovacs, A., Konings, R.J.M., Gibson, J.K., Infante, I., and Gagliardi, L. (2015) Quantum chemical calculations and experimental investigations of molecular actinide oxides. *Chemical Reviews (Washington, DC, U. S.)*, **115**, 1725–1759.

116 Armentrout, P.B. and Beauchamp, J.L. (1980) Collision-induced dissociation of UO^+ and UO_2^+ ions. *Chemical Physics*, **50**, 21–25.

117 Gibson, J.K. and Marçalo, J. (2006) New developments in gas-phase actinide ion chemistry. *Coordination Chemistry Reviews*, **250**, 776–783.

118 Gibson, J.K. (1997) Gas-phase f-element organometallic chemistry: Reactions of cyclic hydrocarbons with Th^+, U^+, ThO^+, UO^+, and lanthanide ions, Ln^+. *Organometallics*, **16**, 4214–4222.

119 Gibson, J.K. (2002) Gas-phase chemistry of actinide ions: Probing the distinctive character of the 5f elements. *International Journal of Mass Spectrometry*, **214**, 1–21.

120 Van Stipdonk, M.J., Michelini, M.d.C., Plaviak, A., Martin, D., and Gibson, J.K. (2014) Formation of bare UO_2^{2+} and NUO^+ by fragmentation of gas-phase uranyl-acetonitrile complexes. *Journal of Physical Chemistry A*, **118**, 7838–7846.

121 Lucena, A.F., Odoh, S.O., Zhao, J., Marçalo, J., Schreckenbach, G., and Gibson, J.K. (2014) Oxo-exchange of gas-phase uranyl, neptunyl, and plutonyl with water and methanol. *Inorganic Chemistry*, **53**, 2163–2170.

122 Gong, Y. and Gibson, J.K. (2014) Crown ether complexes of uranyl, neptunyl, and plutonyl: Hydration differentiates inclusion versus outer coordination. *Inorganic Chemistry*, **53**, 5839–5844.

123 Gong, Y., Hu, H.-S., Rao, L., Li, J., and Gibson, J.K. (2013) Experimental and theoretical studies on the fragmentation of gas-phase uranyl-, neptunyl-, and plutonyl-diglycolamide complexes. *Journal of Physical Chemistry A*, **117**, 10544–10550.

124 Vasiliu, M., Peterson, K.A., Gibson, J.K., and Dixon, D.A. (2015) Reliable potential energy surfaces for the reactions of H_2O with ThO_2, PaO_2^+, UO_2^{2+}, and UO_2^+. *Journal of Physical Chemistry A*, **119**, 11422–11431.

125 Becke, A.D. (1993) Density-functional thermochemistry. III. The role of exact exchange. *Journal of Chemical Physics*, **98**, 5648.

126 Lee, C., Yang, W., and Parr, R.G. (1988) Development of the Colle-Salvetti correlation-energy formula into a functional of the electron density. *Physical Review B*, **37**, 785.

127 Perdew, J.P. and Wang, Y. (1992) Accurate and simple analytic representation of the electron gas correlation energy. *Physical Review B*, **45**, 13244–13249.

128 Perdew, J.P., Burke, K., and Ernzerhof, M. (1996) Generalized gradient approximation made simple. *Physical Review Letters*, **77**, 3865–3868.

129 Raghavachari, K., Trucks, G.W., Pople, J.A., and Head-Gordon, M. (1989) A fifth-order perturbation comparison of electron correlation theories. *Chemical Physics Letters*, **157**, 479–483.

130 Roos, B., Taylor, P., and Siegbahn, P.E.M. (1980) A complete active space SCF method (CASSCF) using a density matrix formulated super-CI approach. *Chemical Physics*, **48**, 157–173.

131 Andersson, K., Malmqvist, P.-A., and Roos, B.O. (1992) Second-order perturbation theory with a complete active space self-consistent field reference function. *Journal of Chemical Physics*, **96**, 1218.

132 Andersson, K., Malmqvist, P.A., Roos, B.O., Sadlej, A.J., and Wolinski, K. (1990) Second-order perturbation-theory with a CASSCF reference function. *Journal of Physical Chemistry*, **94**, 5483–5488.

133 Kovacs, A., Infante, I., and Gagliardi, L. (2013) Theoretic study of the electronic spectra of neutral and cationic PaO and PaO_2. *Structural Chemistry*, **24**, 917–925.

134 Roos, B.O., Malmqvist, P.-A., and Gagliardi, L. (2006) Exploring the actinide-actinide bond: Theoretical studies of the chemical bond in Ac_2, Th_2, Pa_2, and U_2. *Journal of the American Chemical Society*, **128**, 17000–17006.

135 Olsen, J., Roos, B.O., Jørgensen, P., and Jensen, H.J.A. (1988) Determinant based configuration interaction algorithms for complete and restricted configuration interaction spaces. *Journal of Chemical Physics*, **89**, 2185.

136 Fleig, T., Olsen, J., and Marian, C.M. (2001) The generalized active space concept for the relativistic treatment of electron correlation. I. Kramers-restricted two-component configuration interaction. *Journal of Chemical Physics*, **114**, 4775–4790.

137 Werner, H.-J. and Knowles, P.J. (1988) An efficient internally contracted multiconfiguration-reference configuration interaction method. *Journal of Chemical Physics*, **89**, 5803–5814.

138 Langhoff, S.R. and Davidson, E.R. (1974) Configuration interaction calculations on the nitrogen molecule. *International Journal of Quantum Chemistry*, **8**, 61–72.

139 Bross, D.H. and Peterson, K.A. (2015) Theoretical spectroscopy study of the low-lying electronic states of UX and UX^+, X = F and Cl. *Journal of Chemical Physics*, **143**, 184313.

140 Dolg, M. and Cao, X. (2009) Accurate relativistic small-core pseudopotentials for actinides. Energy adjustment for uranium and first applications to uranium hydride†. *Journal of Physical Chemistry A*, **113**, 12573–12581.

141 Visscher, L., Eliav, E., and Kaldor, U. (2001) Formulation and implementation of the relativistic Fock-space coupled cluster method for molecules. *Journal of Chemical Physics*, **115**, 9720–9726.

142 Landau, A., Eliav, E., and Kaldor, U. (1999) Intermediate Hamiltonian Fock-space coupled-cluster method. *Chemical Physics Letters*, **313**, 399–403.

143 Infante, I., Eliav, E., Vilkas, M.J., Ishikawa, Y., Kaldor, U., and Visscher, L. (2007) A Fock space coupled cluster study on the electronic structure of the UO_2, UO_2^+, U^{4+}, and U^{5+} species. *Journal of Chemical Physics*, **127**, 124308.

144 Jansen, G. and Hess, B.A. (1989) Revision of the Douglas-Kroll transformation. *Physical Review A*, **39**, 6016.

145 Wolf, A., Reiher, M., and Hess, B.A. (2002) The generalized Douglas-Kroll transformation. *Journal of Chemical Physics*, **117**, 9215–9226.

146 Iliaš, M. and Saue, T. (2007) An infinite-order two-component relativistic Hamiltonian by a simple one-step transformation. *Journal of Chemical Physics*, **126**, 064102.

147 Malmqvist, P.A., Roos, B.O., and Schimmelpfennig, B. (2002) The restricted active space (RAS) state interaction approach with spin-orbit coupling. *Chemical Physics Letters*, **357**, 230–240.

148 Hess, B.A., Marian, C.M., and Peyerimhoff, S.D. (1995) Ab initio calculation of spin-oribit effects in molecules including electron correlation, in *Modern Electronic Structure Theory, Part I*, D.R. Yarkony, Editor. World Scientific, Singapore. pp. 152–278.

149 Hess, B.A., Marian, C.M., Wahlgren, U., and Gropen, O. (1996) A mean-field spin-orbit method applicable to correlated wavefunctions. *Chemical Physics Letters*, **251**, 365–371.

150 Yabushita, S., Zhang, Z., and Pitzer, R.M. (1999) Spin-orbit configuration interaction using the graphical unitary group approach and relativistic core potential and spin-orbit operators. *Journal of Physical Chemistry A*, **103**, 5791–5800.

151 Tyagi, R., Zhang, Z., and Pitzer, R.M. (2014) Electronic spectrum of the UO and UO^+ molecules. *Journal of Physical Chemistry A*, **118**, 11758–11767.

152 Saue, T. (2011) Relativistic Hamiltonians for chemistry: A primer. *ChemPhysChem*, **12**, 3077–3094.

153 Knecht, S., Jensen, H.J.A., and Fleig, T. (2010) Large-scale parallel configuration interaction. II. Two- and four-component double-group general active space implementation with application to BiH. *Journal of Chemical Physics*, **132**, 014108.

154 Visscher, L., Lee, T.J., and Dyall, K.G. (1996) Formulation and implementation of a relativistic unrestricted coupled-cluster method including noniterative connected triples. *Journal of Chemical Physics*, **105**, 8769–8776.

155 van Lenthe, E., Baerends, E.J., and Snijders, J.G. (1993) Relativistic regular two-component Hamiltonians. *Journal of Chemical Physics*, **99**, 4597.

156 Sikkema, J., Visscher, L., Saue, T., and Iliaš, M. (2009) The molecular mean-field approach for correlated relativistic calculations. *Journal of Chemical Physics*, **131**, 124116–.

157 Weigand, A., Cao, X., Hangele, T., and Dolg, M. (2014) Relativistic small-core pseudopotentials for actinium, thorium, and protactinium. *Journal of Physical Chemistry A*, **118**, 2519–2530.

158 Peterson, K.A. and Dyall, K.G. (2015) Gaussian Basis sets for lanthanide and actinide elements: Strategies for their development and use, in *Computational Methods in Lanthanide and Actinide Chemistry*, M. Dolg, Editor. John Wiley & Sons, Chichester, West Sussex, UK. pp. 195–216.

159 Velde, G., Bickelhaupt, F., Baerends, E.J., Guerra, C., van Gisbergen, S., Snijders, J., and Ziegler, T. (2001) Chemistry with ADF. *Journal of Computational Chemistry*, **22**, 931–967.

160 Dyall, K.G. (2007) Relativistic double-zeta, triple-zeta, and quadruple-zeta basis sets for the actinides Ac–Lr. *Theoretical Chemistry Accounts*, **117**, 491–500.

161 Roos, B.O., Lindh, R., Malmqvist, P.A., Veryazov, V., and Widmark, P.O. (2005) New relativistic ANO basis sets for actinide atoms. *Chemical Physics Letters*, **409**, 295–299.

162 Peterson, K.A. (2015) Correlation consistent basis sets for actinides. I. The Th and U atoms. *Journal of Chemical Physics*, **142**, 074105.

163 Feng, R. and Peterson, K.A. (2017) Correlation consistent basis sets for actinides. II. The atoms Ac and Np-Lr. *Journal of Chemical Physics*, **147**, 084108.

164 Feller, D., Peterson, K.A., and Hill, J.G. (2011) On the effectiveness of CCSD(T) complete basis set extrapolations for atomization energies. *Journal of Chemical Physics*, **135**, 044102.

165 Pantazis, D.A. and Neese, F. (2011) All-electron scalar relativistic basis sets for the actinides. *Journal of Chemical Theory and Computation*, **7**, 677–684.

166 Blaudeau, J.-P., Brozell, S.R., Matsika, S., Zhang, Z., and Pitzer, R.M. (2000) Atomic orbital basis sets for use with effective core potentials. *International Journal of Quantum Chemistry*, **77**, 516–520.

167 Christiansen, P.A., Lee, Y.S., and Pitzer, K.S. (1979) Improved ab initio effective core potentials for molecular calculations. *Journal of Chemical Physics*, **71**, 4445–4450.

168 Küchle, W., Dolg, M., Stoll, H., and Preuss, H. (1994) Energy-adjusted pseudopotentials for the actinides – parameter sets and test calculations for thorium and thorium monoxide. *Journal of Chemical Physics*, **100**, 7535–7542.

169 Cao, X. and Dolg, M. (2004) Segmented contraction scheme for small-core actinide pseudopotential basis sets. *Journal of Molecular Structure: THEOCHEM*, **673**, 203–209.

170 Bross, D.H. and Peterson, K.A. (2014) Composite thermochemistry of gas phase U(VI)-containing molecules. *Journal of Chemical Physics*, **141**, 244308.

171 Lindh, R., Molcas 8.0: F. Aquilante, J. Autschbach, R. K. Carlson, L. F. Chibotaru, M. G. Delcey, L. De Vico, I. Fdez. Galvan, N. Ferré, L. M. Frutos, L. Gagliardi, M. Garavelli, A. Giussani, C. E. Hoyer, G. Li Manni, H. Lischka, D. Ma, P Å Malmqvist, T. Müller, A. Nenov, M. Olivucci, T. B. Pedersen, D. Peng, F. Plasser, B. Pritchard, M. Reiher, I. Rivalta, I. Schapiro, J. Segarra-Marti, M. Stenrup, D. G Truhlar, L. Ungur, A. Valentini, S. Vancoillie, V. Veryazov, V. P. Vysotskiy, O. Weingart, F. Zapata, R. Lindh (2016). MOLCAS 8. *Journal of Computational Chemistry*, **37**, 506–541.

172 Werner, H.-J., MOLPRO, version 2015.1, a package of ab initio programs, H.-J. Werner, P. J. Knowles, G. Knizia, F. R. Manby, M. Schütz, P. Celani, W. Györffy, D. Kats, T. Korona, R. Lindh, A. Mitrushenkov, G. Rauhut, K. R. Shamasundar, T. B. Adler, R. D. Amos, A. Bernhardsson, A. Berning, D. L. Cooper, M. J. O. Deegan, A. J. Dobbyn, F. Eckert, E. Goll, C. Hampel, A. Hesselmann, G. Hetzer, T. Hrenar, G. Jansen, C. Köppl, Y. Liu, A. W. Lloyd, R. A. Mata, A. J. May, S. J. McNicholas, W. Meyer, M. E. Mura, A. Nicklass, D. P. O'Neill, P. Palmieri, D. Peng, K. Pflüger, R. Pitzer,

M. Reiher, T. Shiozaki, H. Stoll, A. J. Stone, R. Tarroni, T. Thorsteinsson, and M. Wang, see http://www.molpro.net.

173 Visscher, L., Jensen, H.J.A., Bast, R., and Saue, T., DIRAC, a relativistic ab initio electronic structure program, Release DIRAC15 (2015), written by R. Bast, T. Saue, L. Visscher, and H. J. Aa. Jensen, with contributions from V. Bakken, K. G. Dyall, S. Dubillard, U. Ekstroem, E. Eliav, T. Enevoldsen, E. Fasshauer, T. Fleig, O. Fossgaard, A. S. P. Gomes, T. Helgaker, J. Henriksson, M. Iliaš, Ch. R. Jacob, S. Knecht, S. Komorovsky, O. Kullie, J. K. Laerdahl, C. V. Larsen, Y. S. Lee, H. S. Nataraj, M. K. Nayak, P. Norman, G. Olejniczak, J. Olsen, Y. C. Park, J. K. Pedersen, M. Pernpointner, R. Di Remigio, K. Ruud, P. Salek, B. Schimmelpfennig, J. Sikkema, A. J. Thorvaldsen, J. Thyssen, J. van Stralen, S. Villaume, O. Visser, T. Winther, and S. Yamamoto (see http://www.diracprogram.org).

174 Fox, D.J., Gaussian 09, Revision E.01, M. J. Frisch, G. W. Trucks, H. B. Schlegel, G. E. Scuseria, M. A. Robb, J. R. Cheeseman, G. Scalmani, V. Barone, B. Mennucci, G. A. Petersson, H. Nakatsuji, M. Caricato, X. Li, H. P. Hratchian, A. F. Izmaylov, J. Bloino, G. Zheng, J. L. Sonnenberg, M. Hada, M. Ehara, K. Toyota, R. Fukuda, J. Hasegawa, M. Ishida, T. Nakajima, Y. Honda, O. Kitao, H. Nakai, T. Vreven, J. A. Montgomery, Jr., J. E. Peralta, F. Ogliaro, M. Bearpark, J. J. Heyd, E. Brothers, K. N. Kudin, V. N. Staroverov, R. Kobayashi, J. Normand, K. Raghavachari, A. Rendell, J. C. Burant, S. S. Iyengar, J. Tomasi, M. Cossi, N. Rega, J. M. Millam, M. Klene, J. E. Knox, J. B. Cross, V. Bakken, C. Adamo, J. Jaramillo, R. Gomperts, R. E. Stratmann, O. Yazyev, A. J. Austin, R. Cammi, C. Pomelli, J. W. Ochterski, R. L. Martin, K. Morokuma, V. G. Zakrzewski, G. A. Voth, P. Salvador, J. J. Dannenberg, S. Dapprich, A. D. Daniels, Ö. Farkas, J. B. Foresman, J. V. Ortiz, J. Cioslowski, and D. J. Fox, Gaussian, Inc., Wallingford CT, 2009.

175 Peterson, K.A., Feller, D., and Dixon, D.A. (2012) Chemical accuracy in ab initio thermochemistry and spectroscopy: Current strategies and future challenges. *Theoretical Chemistry Accounts*, **131**, 1079.

176 Schuurman, M.S., Muir, S.R., Allen, W.D., and Schaefer, H.F., III, (2004) Towamochemistry: Focal point analysis of the heat of formation of NCO and [H,N,C,O] isomers. *Journal of Chemical Physics*, **120**, 11586.

177 Karton, A., Rabinovich, E., Martin, J.M.L., and Ruscic, B. (2006) W4 theory for computational thermochemistry: In pursuit of confident sub-kJ/mol predictions. *Journal of Chemical Physics*, **125**, 144108.

178 Harding, M.E., Vazquez, J., Ruscic, B., Wilson, A.K., Gauss, J., and Stanton, J.F. (2008) High-accuracy extrapolated ab initio thermochemistry. III. Additional improvements and overview. *Journal of Chemical Physics*, **128**, 114111.

179 DeYonker, N.J., Grimes, T., Yokel, S., Dinescu, A., Mintz, B., Cundari, T.R., and Wilson, A.K. (2006) The correlation-consistent composite approach: Application to the G3/99 test set. *Journal of Chemical Physics*, **125**, 104111.

180 Feller, D., Peterson, K.A., and Dixon, D.A. (2008) A survey of factors contributing to accurate theoretical predictions of atomization energies and molecular structures. *Journal of Chemical Physics*, **129**, 204105.

181 Kendall, R.A., Dunning Jr, T.H., and Harrison, R.J. (1992) Electron affinities of the first-row atoms revisited. Systematic basis sets and wave functions. *Journal of Chemical Physics*, **96**, 6796.

182 Dunning Jr, T.H. (1989) Gaussian basis sets for use in correlated molecular calculations. I. The atoms boron through neon and hydrogen. *Journal of Chemical Physics*, **90**, 1007.

183 de Jong, W.A., Harrison, R.J., and Dixon, D.A. (2001) Parallel Douglas-Kroll energy and gradients in NWChem: Estimating scalar relativistic effects using Douglas-Kroll contracted basis sets. *Journal of Chemical Physics*, **114**, 48–53.

184 Karton, A. and Martin, J.M.L. (2006) Comment on: "Estimating the Hartree-Fock limit from finite basis set calculations" [Jensen F (2005) *Theor Chem Acc* 113, 267]. *Theoretical Chemistry Accounts*, **115**, 330–333.

185 Peterson, K.A. and Dunning, T.H., Jr. (2002) Accurate correlation consistent basis sets for molecular core-valence correlation effects. The second row atoms Al–Ar, and the first row atoms B–Ne revisited. *Journal of Chemical Physics*, **117**, 10548–10560.

186 Martin, J.M.L. (1996) Ab initio total atomization energies of small molecules – Towards the basis set limit. *Chemical Physics Letters*, **259**, 669–678.

187 Pyykkö, P. and Zhao, L.-B. (2003) Search for effective local model potentials for simulation of quantum electrodynamic effects in relativistic calculations. *Journal of Physics B: Atomic, Molecular and Optical Physics*, **36**, 1469.

188 Hildenbrand, D.L. and Lau, K.H. (1991) Redetermination of the thermochemistry of gaseous UF_5, UF_2, and UF. *Journal of Chemical Physics*, **94**, 1420–1425.

189 Noga, J. and Bartlett, R.J. (1987) The full CCSDT model for molecular electronic structure. *Journal of Chemical Physics*, **86**, 7041–7050.

190 Watts, J.D. and Bartlett, R.J. (1990) The coupled-cluster single, double, and triple excitation model for open-shell single reference functions. *Journal of Chemical Physics*, **93**, 6104–6105.

191 Kucharski, S.A. and Bartlett, R.J. (1992) The coupled-cluster single, double, triple, and quadruple excitation method. *Journal of Chemical Physics*, **97**, 4282–4288.

192 Kucharski, S.A. and Bartlett, R.J. (1998) Noniterative energy corrections through fifth-order to the coupled cluster singles and doubles method. *Journal of Chemical Physics*, **108**, 5243.

193 Cox, R.M., Citir, M., Armentrout, P.B., Battey, S.R., and Peterson, K.A. (2016) Bond energies of ThO^+ and ThC^+: A guided ion beam and quantum chemical investigation of the reactions of thorium cation with O_2 and CO. *Journal of Chemical Physics*, accepted.

194 Guillaumont, R., Fanghånel, T., Neck, V., Fuger, J., Palmer, D.A., Grenthe, I., and Rand, M.H. (2003) *Chemical Thermodynamics 5: Update on the Chemical Thermodynamics of Uranium, Neptunium, Plutonium, Americium and Technetium*. Amsterdam: Elsevier.

195 Thanthiriwatte, K.S., Wang, X., Andrews, L., Dixon, D.A., Metzger, J., Vent-Schmidt, T., and Riedel, S. (2014) Properties of ThF_x from infrared spectra in solid argon and neon with supporting electronic structure and thermochemical calculations. *Journal of Physical Chemistry A*, **118**, 2107–2119.

196 Peralta, J.E., Batista, E.R., Scuseria, G.E., and Martin, R.L. (2005) All-electron hybrid density functional calculations on UF_n and UCl_n (n = 1-6). *Journal of Chemical Theory and Computation*, **1**, 612–616.

197 Adamo, C. and Barone, V. (1999) Toward reliable density functional methods without adjustable parameters: The PBE0 model. *Journal of Chemical Physics*, **110**, 6158–6170.

198 Ernzerhof, M. and Scuseria, G.E. (1999) Assessment of the Perdew–Burke–Ernzerhof exchange-correlation functional. *Journal of Chemical Physics*, **110**, 5029–5036.

199 Goncharov, V. and Heaven, M.C. (2006) Spectroscopy of the ground and low-lying excited states of ThO^+. *Journal of Chemical Physics*, **124**, 064312.

200 Infante, I., Kovacs, A., La Macchia, G., Shahi, A.R.M., Gibson, J.K., and Gagliardi, L. (2010) Ionization energies for the actinide mono- and dioxides series, from Th to Cm: Theory versus experiment. *Journal of Physical Chemistry A*, **114**, 6007–6015.

201 Marçalo, J. and Gibson, J.K. (2009) Gas-phase energetics of actinide oxides: An assessment of neutral and cationic monoxides and dioxides from thorium to curium. *Journal of Physical Chemistry A*, **113**, 12599–12606.

202 Averkiev, B., Mantina, M., Valero, R., Infante, I., Kovacs, A., Truhlar, D., and Gagliardi, L. (2011) How accurate are electronic structure methods for actinoid chemistry? *Theoretical Chemistry Accounts*, **129**, 657–666.

203 Paulovič, J., Gagliardi, L., Dyke, J.M., and Hirao, K. (2005) A theoretical study of the gas-phase chemi-ionization reaction between uranium and oxygen atoms. *Journal of Chemical Physics*, **122**, 144317.

204 Jackson, V.E., Craciun, R., Dixon, D.A., Peterson, K.A., and de Jong, W.A. (2008) Prediction of vibrational frequencies of UO_2^{2+} at the CCSD(T) level. *Journal of Physical Chemistry A*, **112**, 4095–4099.

205 Odoh, S.O. and Schreckenbach, G. (2010) Performance of relativistic effective core potentials in DFT calculations on Actinide compounds. *Journal of Physical Chemistry A*, **114**, 1957–1963.

206 Gagliardi, L. and Roos, B.O. (2000) Uranium triatomic compounds XUY (X,Y = C,N,O): A combined multiconfigurational second-order perturbation and density functional study. *Chemical Physics Letters*, **331**, 229–234.

207 Zhou, M.F., Andrews, L., Li, J., and Bursten, B.E. (1999) Reaction of laser-ablated uranium atoms with CO: Infrared spectra of the CUO, CUO^-, OUCCO, (eta(2)-C-2) UO_2,-and $U(CO)_x$ (x = 1-6) molecules in solid neon. *Journal of the American Chemical Society*, **121**, 9712–9721.

208 Andrews, L., Liang, B.Y., Li, J., and Bursten, B.E. (2000) Ground-state reversal by matrix interaction: Electronic states and vibrational frequencies of CUO in solid argon and neon. *Angewandte Chemie-International Edition*, **39**, 4565.

209 Li, J., Bursten, B.E., Liang, B.Y., and Andrews, L. (2002) Noble gas-actinide compounds: Complexation of the CUO molecule by Ar, Kr, and Xe atoms in noble gas matrices. *Science*, **295**, 2242–2245.

210 Roos, B.O., Widmark, P.O., and Gagliardi, L. (2003) The ground state and electronic spectrum of CUO: A mystery. *Faraday Discussions*, **124**, 57–62.

211 Infante, I. and Visscher, L. (2004) The importance of spin-orbit coupling and electron correlation in the rationalization of the ground state of the CUO molecule. *Journal of Chemical Physics*, **121**, 5783–5788.

212 Yang, T., Tyagi, R., Zhang, Z., and Pitzer, R.M. (2009) Configuration interaction studies on the electronic states of the CUO molecule. *Molecular Physics*, **107**, 1193–1195.

213 Malli, G.L., da Silva, A.B.F., and Ishikawa, Y. (1993) Universal Gaussian basis set for accurate ab initio relativistic Dirac-Fock calculations. *Physical Review A*, **47**, 143–146.

214 Thanthiriwatte, K.S., Vasiliu, M., Battey, S.R., Lu, Q., Peterson, K.A., Andrews, L., and Dixon, D.A. (2015) Gas phase properties of MX_2 and MX_4 (X = F, Cl) for M = Group 4, Group 14, Cerium, and Thorium. *Journal of Physical Chemistry A*, **119**, 5790–5803.